Emanuel Karl Peter

ENHANCED SAMPLING TECHNIQUES FOR PROTEIN FOLDING SIMULATIONS

1. INTRODUCTION

Proteins fold into a unique 3-dimensional structure after they have been expressed by the Ribosome in the living cell. The structure and stability of a protein are primarily determined by its amino acid sequence, which also controls its function in intra- and extra-cellular processes. With the development of experimental techniques, i.e. X-ray crystallography and solution nuclear magnetic resonance (NMR) techniques, structural information of proteins on atomic resolution became broadly accessible. Based on this structural information, an abundance of biochemical questions could be resolved, e.g. the elucidation of G protein coupled receptor (GPCR) structures which was awarded with the Nobel prize in Chemistry in 2012. GPCRs are cell-receptors for ligands, including light-sensitive compounds, odor-molecules, pheromones, hormones and neurotransmitters. Thus, an understanding of GPCR structure and function opened the gateway to a vast number of treatment options of various diseases [1]. At present, over 100.000 protein structures have been determined and are available from the RCSB protein data bank [2]. Despite this huge amount of available information based on experiments, proteins are dynamic in order to be able to execute their function, i.e. their conformation space (the number of 3-dimensional structures accessible to the protein at a defined temperature) is larger than the experimentally defined native state. Additionally, the effect of single mutations (exchanges of amino acids in the protein sequence) can dramatically affect the structure of proteins and change their function. For example, pathogenic mutations such as the Arctic Amyloid Precursor Protein (APP) mutation E693G, have been detected to cause an increased risk for a severe form of Alzheimer s disease in a Swedish family [3]. In order to understand protein function and the effect of mutations, pathways of protein folding, i.e. the process of structure-formation after protein expression, have to be investigated. For these studies of protein dynamics (conformation space) and folding pathways on an atomistic level, computational methods have emerged as a complementary tool to experiments.

As it has been stated in Levinthal s paradox, the protein folding pathway cannot be a combinatorial process, i.e. the search of the polypeptide chain for its native conformer has to be directed and is tens of orders of magnitude faster than any combinatorial process. In this way, a reaction consisting of combinatorial search problems would contradict the experimental observation of comparably short time-scales of protein folding reactions [4, 5]. Instead, the folding process is dependent on conformation-states accessible from the instantaneous configuration including the polypeptide chain, the surrounding solvent and electrolytes. In other words, starting from one instantaneous configuration (at time t) only a limited number of new configurations are available at a time t+dt, while structurally independent permutations for finding a new conformer are impossible. In specific cases, e.g. ultra-fast folding proteins, the number of newly accessible structures in a period from t to t+dt throughout the folding pathway is restricted to a extremely low number. Subsequently, if we observe any protein in a hypothetically infinite time-frame, the folded state of a polypeptide chain (corresponding to the experimental structure) is then the ensemble of conformations (a collection of structures with the same structural properties) occurring with the highest probability. From a thermodynamic perspective, this ensemble of folded configurations (with the largest occurrence) in the native state corresponds to the global free energy minimum for this specific protein. It is worth mentioning, that the system containing the peptide is at equilibrium, while the protein in this very folding process might dissipate energy into its surrounding. In other words, the system might be locally out of equilibrium at a defined time-frame, but not globally. This behaviour is also reflected by changes in the specific temperature dependent heat capacities obtained in simulations.

A vast number of theories for protein folding have been developed in the last decades, while very few developments are actually based on first principles, i.e. on simplest and irreducible physical conjectures. At present, there are 2 models representing different boundary cases of the rate-limiting event in protein folding reactions : First, the diffusion collision model and second, the nucleation condensation model. In the diffusion collision model, minor structural motifs, i.e. spatially separated sub-structures, which already contain partial native secondary or tertiary structures (depending on the size of the protein), are formed slowly after the expression by the Ribosome. Subsequently, the different motifs diffuse and collide fast, driven by thermal fluctuations, until the complete native tertiary structure has aligned. The nucleation condensation model assumes that the protein forms a nucleus in a slow process at the beginning. Through the formation of this nucleus, the global tertiary structure is already pre-defined. This nucleation event is then

Dr. rer. nat. Emanuel Karl Peter
Institute of Computational Science, Faculty of Informatics
University of Lugano
Via Giuseppe Buffi 12, 6900 Lugano, Switzerland
Telefon: +41 58 666 4980
E-Mail: petere@usi.ch

followed by a fast condensation -process, consisting of the subsequent formation of structural elements (motifs) around this nucleus leading to the native state. It should be noted, that actual folding pathways might be described by more complex intermediate models, e.g. an initial diffusion-collision process might lead to a nucleation event, followed by condensation and the formation of the native structure. Alternatively, large proteins (> 400 amino-acids) might react through several local nucleation-condensation mechanisms, but globally within one single diffusion-collision process.

Most prominent in the description of protein folding and its theory are free energy landscapes (FEL). A free energy landscape (FEL) can be defined as a multi-dimensional space, in which each coordinate (a vector with a sufficient number of defining quantities, usually only 2 order parameters for a 3-dimensional FEL) is associated to a protein-specific free energy (probability), i.e. the occurrence with which this coordinate is accessed by the protein system (see Figure 1). In terms of computer-simulations, protein specific properties, e.g. the radius of gyration or other order parameters (protein specific distances), serve as quantities to express the coordinate space and the associated probabilities (occurrences) within each FEL [6]. As a remark, it has to be mentioned that the FEL is always associated with the Boltzmann-distribution of the system. In order to effectively determine any FEL, the condition that the simulated time-average is equal to the Boltzmann distributed average (ensemble average) has to be approximately fulfilled. In terms of computer-simulations, algorithm-specific convergence criteria have emerged, which qualitatively allow the statement of a given equality between time- and ensemble average. At present, only small peptide systems up to proteins of moderate size (~120 aminoacids) can be simulated with the use of enhanced sampling techniques, so that the ensemble average can approximately be reached. A wrong out of equilibrium starting configuration with high potential energies (atomic overlaps) might violate this principle already at the beginning of the simulation, even if the integration algorithm can propagate the system.

In the case of small stable folding peptides with a size lower than 100 amino-acids, the folded state of any protein can be found in its free energy minimum (ΔG = - 2-4 k_BT). As a consequence, the folding pathway of this type of protein occurs downhill along a funnel-shaped FEL (see Figure 2). A theory of a funneled FEL also explains that folding pathways are equally probable from any possible conformation of the peptide in the unfolded ensemble with approximately similar folding kinetics. The funnel-theory has been confirmed in experiments based on temperature jump transient circular-dichroism (CD) and transient tryptophan-fluorescence spectroscopy, while it should be mentioned that these experiments contained the information of folding of an ensemble of small and stable peptides [7]. In these experiments, mono-exponential decay kinetics indicated a direct folding reaction from the unfolded to the folded state with one single effective barrier (~1-2 k_BT) in between both states. From a computational perspective, this effective barrier is a cumulative sum of small barriers along a rough, funnelled FEL. It should as well be mentioned here, that there are exceptions from this theory. In general, larger proteins with a size larger than 150 aminoacids as well as protein complexes contain very complex FELs. Other examples, where FELs become very complex, are assemblies of intrinsically disordered proteins (IDPs), processes of chaperone assisted folding, and allosteric regulation, i.e. signal processes, in which the FEL changes according to external factors, e.g. light, oxygen, ligands etc. [8, 9, 82]. Another exception are proteins which execute their function between many metastable states with barrier-heights of ~0.5-1 k_BT. In this case, the
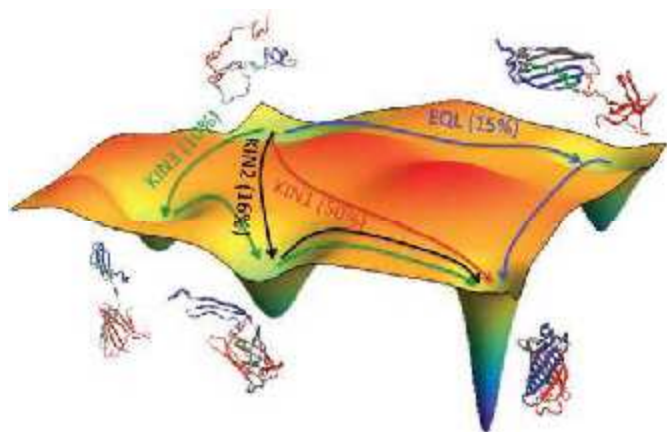

Fig. 1: Example of a folding free energy landscape (FEL) of the green fluorescent protein (GFP). The protein can be captured in many different topological traps, i.e. metastable states along its folding pathway. The different routes observed in folding simulations are indicated by arrows. Representative structures of the different metastable states are shown in this figure. The kinetic traps and metastable minima cause the time-scale problem in protein folding simulations and necessitate the development of enhanced sampling techniques, which are presented in this article.
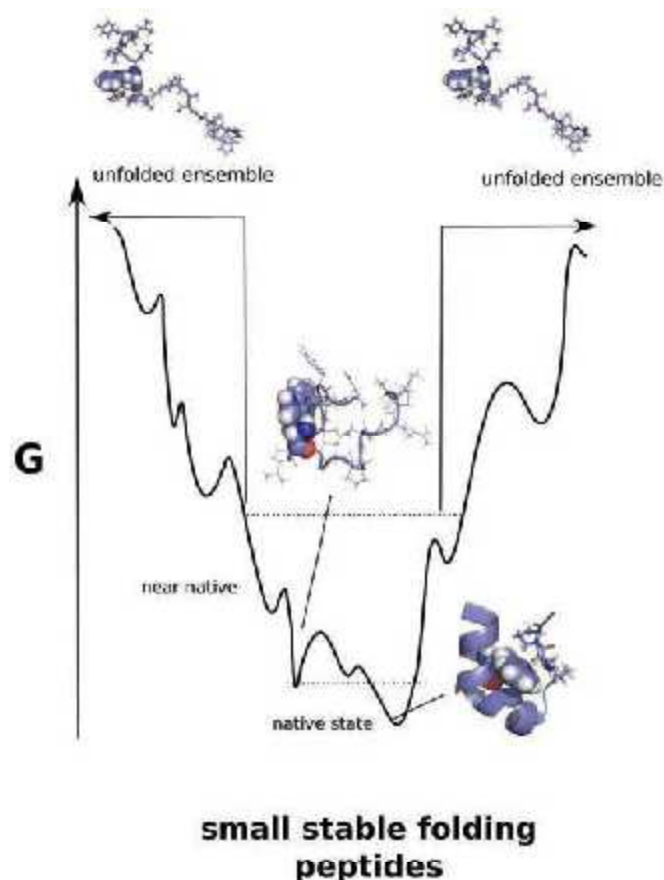

Fig. 2: Schematic pictures of free-energy profiles in protein-folding and dynamics in the case of small stable folding peptides, e.g. TrpCage [75].

proteins do not reach their global FEL minimum (e.g. the dysfunctional denatured state) which is separated by evolutionarily optimised high free energy barriers (~3-5 k_BT). However, as mentioned before, it can be generally assumed that any FEL on an atomistic level is inherently rough, which means that it contains many metastable minima with comparably small barriers of ~0.1-0.5 k_BT between the unfolded and the global FEL-minima of the protein. These metastable minima can be caused by steric effects along the peptide chain, which are characterised as barriers in conformation enthalpy and conformation entropy. While enthalpic effects consist mainly of non-covalent effects like hydrogen bonds (H-bond) and hydrophobic interactions within the protein, the conformation entropy of the polypeptide chain counteracts folding and nucleation. The same thermodynamic driving forces account for the interaction of the protein with the solvent, described by the solvation free energy and the solvent viscosity which restricts the diffusion of the polypeptide chain. In general, the hydrophobic effect represents the main stabilising force for the folded state of proteins and is one of the driving forces for nucleation, i.e. the formation of the hydrophobic core of proteins [10]. These effects cause an inherent roughness of the FEL, and the evolution of the system is affected by barriers in free energy. Thus, the rate-limiting processes are defined by rare events, in which the system can change from one metastable state into another state along the FEL [11].

Molecular dynamics (MD) is a method, which propagates a particle based (in this case atomistic) system in time using Newton s second law of motion. Using a finite time-integration approach, the potential energy gradients in the system are calculated for each time-step (1-2 femtoseconds). The potential energy in the system are usually described by bonded and non-bonded pairwise interactions, which can be separated into van der Waals (Lennard-Jones potential) and electrostatic interactions (Coulomb potential) on the basis of a classical approximation of molecular interactions. Each potential energy parameter is conventionally derived from quantum chemical calculations, and then (in certain cases) adapted to fit to specific (temperature-dependent (!)) molecular properties (dipole moments, static dielectric permittivities, diffusion-coefficients, isothermal compressibilities, phase-partition coefficients etc.). These parameter sets are collected in widely used forcefields, e.g. AMBER03, CHARMM27, OPLS-AA, GROMOS96 ...etc.

MD simulations have emerged as a common tool to investigate pathways of folding and for the prediction of protein structure [12, 13, 14]. However, since the dynamics of proteins evolves along a complex FEL, conventional MD is severely affected by the timescale problem in the description of proteins [15]. In other words, the equilibrium fluctuations in conventional MD allow only rarely a transition of the protein system to cross free energy barriers along its rough FEL. Thus, conventional MD trajectories (coordinates as function of simulated time) can describe only parts of the conformation space (FEL) at moderate computational cost. Recently, a number of developments have been made with the goal to enhance sampling of protein dynamics and protein folding in general. In this article, we will introduce replica exchange MD, Metadynamics and hybrid MD/kinetic Monte Carlo techniques (MD-kMC) for the enhanced sampling in protein folding simulations.

1.1 REPLICA EXCHANGE MOLECULAR DYNAMICS

Replica Exchange Molecular Dynamics (REMD) is a method which simulates the same starting configuration (protein, water) at various temperatures in parallel Molecular Dynamics Simulations (replicas). For example, the replica with index 0 is propagated at room-temperature, and replica(1) at T=302 K, while the highest replica(N) is simulated at T=450 K. This means that the identical starting configuration is replicated and propagated simultaneously in parallel at various temperatures (see Figure 3). At a given interval, e.g. every 1000 integration steps, an exchange is attempted between 2 neighbouring replicas depending on a probability expressed by a Boltzmann-factor, i.e. the exponent of the negative product of the differences between both instantaneous potential energies and the reciprocal temperatures from each replica. If an exchange is permitted according to this criterion, the coordinates and velocities are exchanged. That means, that after an exchange between replica(0) and replica(1) at t>t(exchange), replica(0) will propagate the coordinates of replica(1), while replica(1) will simulate the configuration of replica(0) obtained at t(exchange) [16, 17]. In popular simulation packages an exchange between all replicas with even and odd indices is attempted (0<->1, 2<->3,) at an even exchange attempt, while in each subsequent trial exchanges between odd and even replica-indices are attempted (1<->2, 3<->4,). As a final result, the accumulated trajectories of each replica contain the ensemble (Boltzmann-distributed) information of the peptide system at the related replica-temperature. It should be mentioned here, that time-dependent dynamic information is lost through the exchange process, but the conformation-averaging process for each replica is highly accelerated. This process can be also understood in terms of a repeated Boltzmann-weighted simulated annealing (SA) process, while the detailed balance condition ensures that each replica remains within its Boltzmann-distributed ensemble average, in contrast to SA. In other words, one replica (e.g. replica(0)) follows a conven-
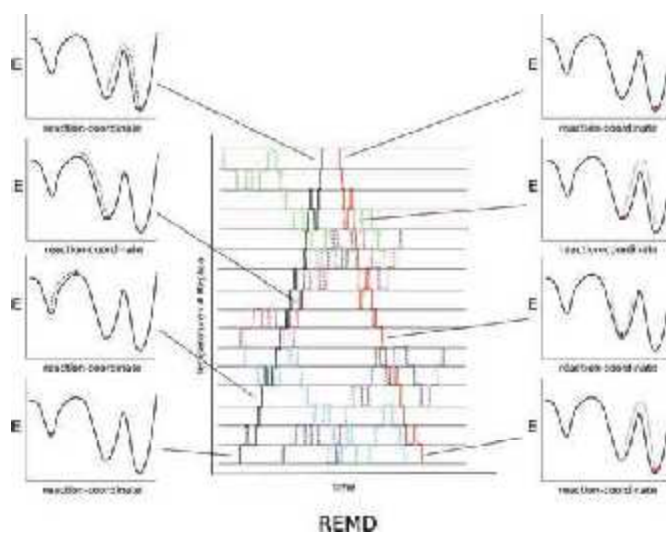

Fig. 3: Schematic picture of the REMD method. The system is simulated in parallel molecular dynamics replicas with rising temperature. The configuration starting at the lowest temperature travels within this temperature space. At high temperature, the probability to reach different low-energy states is increased. Thus, sampling is enhanced and the conformation space is explored faster than with conventional MD.

tional MD-propagation till the time of an exchange-attempt. At the time of an attempt, a random conformation change (a Monte-Carlo move) generated by the neighbouring replica(1) in the prior sampling period is proposed, which is accepted in the case if the Boltzmann-criterion is fulfilled. In the case of acceptance, replica(0) continues to sample the configuration of replica(1) at temperature(0). Through this REMD procedure, the conformation space of a peptide system can be efficiently sampled at each individual temperature simultaneously, i.e. the folding behaviour of a protein at room-temperature can be obtained, but at the same time also at all other individual temperature-related Boltzmann-distributions (i.e. the temperature dependent FELs for each replica). Usually, the replica temperatures are chosen such that the exchange probability is sufficiently high (~10 %), i.e. there will be a sufficient exchange between the parallel replicas. This exchange probability primarily depends on the overlap of distributions of potential energies in neighbouring replicas, which is correlated with the temperatures in both replicas (e.g. in the case of an exchange probability of 100 % between replicas 1 and 2, the instantaneous energy difference ($E_1 - E_2$) is equal to zero or negative between the 2 replicas). In conventional REMD, the replicas rise in temperature with increasing replica index, and each replica performs different dynamics in a different thermodynamic state. This thermodynamic state of the system can be characterised by its average temperature and the associated entropy in the system. With increasing temperature, the entropy in the system rises, resulting in a larger number of possible configurations in the system. Therefore, an exchange between higher and lower replicas enables fast sampling of the conformation ensemble at each individual temperature. The quality of sampling in a REMD simulation is measured by the number of swaps of each replica, and how often the highest replica is visited by the replica with the lowest index.

REMD has emerged as a major technique for enhanced sampling and is widely used. However, the demanding question when REMD simulations have converged has not been fully resolved, yet [18]. As a measure for the convergence of REMD simulations, quantities such as the root-mean square deviation to the native structure (the structure with the highest occurrence), other order parameters (native contact order, secondary structure content, intra-peptide distances, radius of gyration) and the number of native hydrogen-bonds have been proposed [19]. Clearly, a unique measure for convergence is the conformation entropy and folding free energy resulting from the probability distributions and the root-mean square fluctuation of the protein. In the case if no experimental data (folding free energies, structural data) or reference simulations exist, specific analyses and statistical tests should be performed to probe the simulations for statistical consistency and convergence of statistical quantities related to the conformation entropy [20]. Finally, we note that REMD becomes computationally demanding the more particles are contained in the system, since the overlap in the potential energies decreases and the temperature differences have to be decreased so that the exchange rate remains sufficiently high. A number of developments have been made to enhance the sampling efficiency of REMD, and to extend it to other ensembles (for example the NPT - constant particle number, constant pressure, constant
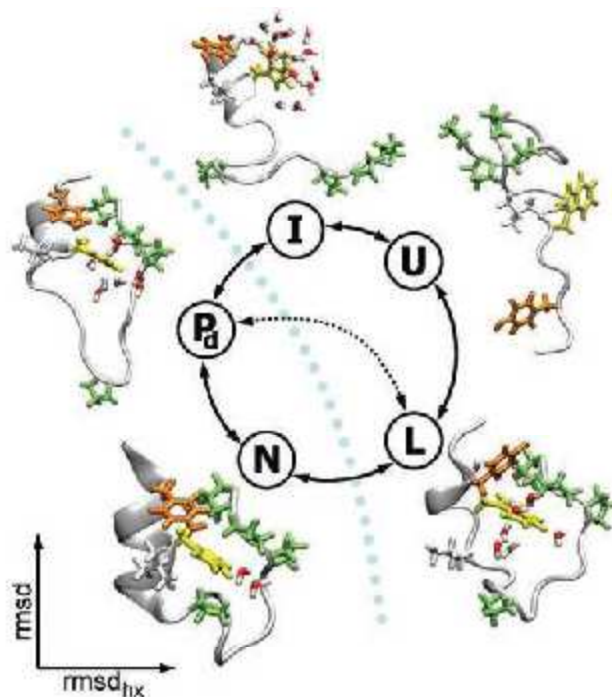

Fig. 4: Folding intermediates of the TrpCage mini-protein sampled in REMD simulations [19]. It has been found that TrpCage folds along both nucleation-condensation and diffusion-collision pathways. The central Trp-residue and the adjacent Poly-Proline helix facilitates a fast collapse into the native structure.

temperature - ensemble.) [21-47]. REMD has been used for the prediction of FELs of the TrpCage miniprotein (see Figure 4) [18], the TrpZipper β-stranded peptides and GB1 [48-54]. In another work, the influence of the solvent on folding and unfolding of TrpCage has been investigated [51, 52]. A number of studies have been performed on the protein folding problem in vicinity of surfaces [53-54]. Finally, we also mention that REMD also has been used in combination with coarse-graining techniques for the simulation of protein aggregation [55].

1.2 METADYNAMICS

Metadynamics is a technique which enhances sampling in MD simulations and reconstructs the FEL of a system as function of few selected degrees of freedom, i.e. collective variables (CVs). In metadynamics the MD-simulation is accelerated by a history dependent bias potential, which is constructed in the space of the CVs (see Figure 5). For example, the CV for sodium chloride would be the center to center distance between both ions, corresponding to ion-ion association and dissociation processes. In the case of a plain di-alanine peptide, the dihedral angle along the amide-bond represents a CV for this system, reflecting the reaction coordinate for isomerization processes. In plain words, the system is forced by the bias to permanently visit new states along the defined CV, e.g. a sodium ion is slightly driven in a predefined way to change its relative position towards chloride to either associate or dissociate. Thereby, the simulation is highly accelerated, because the system, e.g. the sodium ion, permanently tends to leave minima along the FEL and searches for new states. The deeper the FEL minimum, the longer the system stays in this region, but as the bias (in the form of
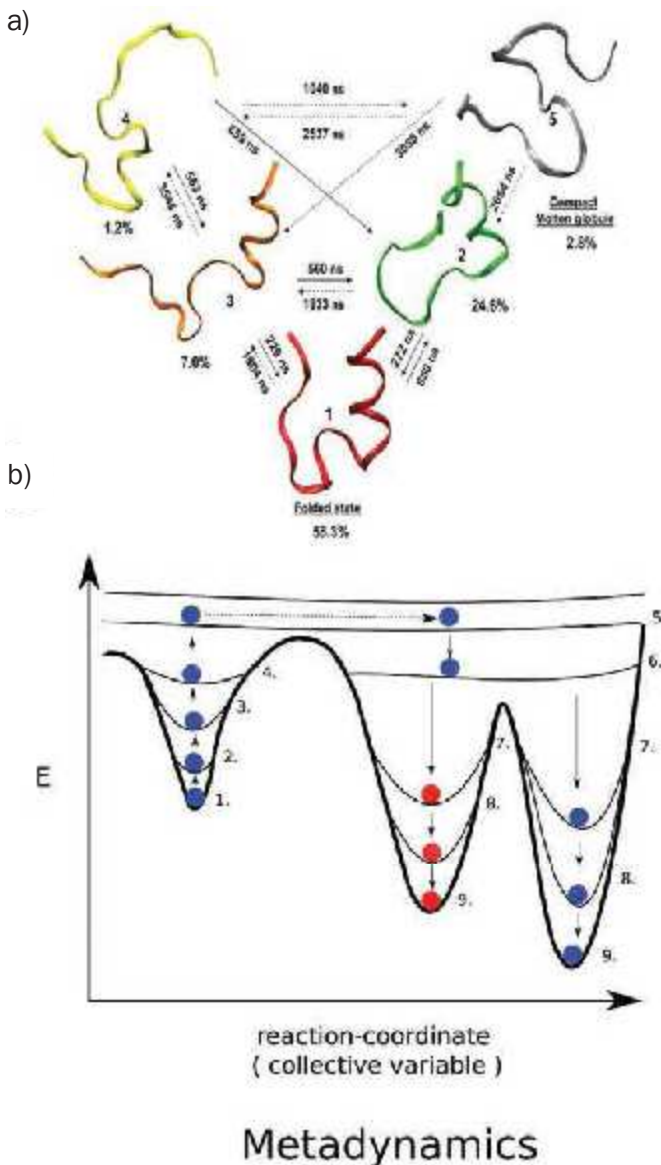
a)

b)

reaction-coordinate
(collective variable)

Metadynamics

Fig. 5: (a) The kinetic pathways of TrpCage-folding using multiple-bias Metadynamics (a combination of REMD and Metadynamics) [46]. (b) Schematic 2-dimensional potential energy profile with the instantaneous conformation indicated in blue and red colored spheres. In the course of the Metadynamics simulation, the potential-energy space is systematically filled up with Gaussians, and the system can escape metastable FEL minima. Subsequently, after the estimated conformation is reached (at which no barriers exist), the FEL is reconstructed in a stepwise process. Essential in Metadynamics is the appropriate choice of collective variables to define the reaction coordinate (collective variable).

Gaussians) has filled this minimum, the system will be driven towards new states. A number of methods belong to this class of methods, including umbrella sampling [56], local elevation [57], conformational flooding [58, 59], adaptive force bias [60], steered MD [61] and self-healing umbrella sampling [62]. The external history dependent bias potential is added to the Hamiltonian of the system. It is written in form of a sum of Gaussians deposited along the system trajectory in CV-space, which discourages the system to revisit sampled configurations. The bias is applied continuously either through an extended Lagrange formalism [63] or the bias acts directly on the microscopic coordinates in the system. In that way, Metadynamics accelerates the sampling of rare events and enables the system to escape from local free energy minima. Metadynamics does not require

an a priori knowledge of the free energy landscape and explores the regions low in free energy first. At the final stage, the applied bias potential provides an estimate of the un-biased free energy. This is possible, since the history dependent bias potential can be successively substracted again from the flooded potential-energy state and the histogram-dependent free energies of all visited states of the FEL. Although the formalism is suitable for the acceleration of simulations and the determination of the free energy, there are 2 major problems in this technique. First, the bias potential does not lead automatically to convergence in sampling of the entire FEL, but can lead to oscillations in one certain region of the FEL. Second, the identification of a set of CVs for a complex process is far from being trivial. The selection of any CV has to distinguish between the initial and the final state of a simulation and has to describe the relevant intermediates. Furthermore, it has to describe every slow mode in the system. Finally, the number of CVs selected to describe the system has to be as small as possible. Choosing the correct CV is based on an understanding of the physical problem or the underlying chemistry and might include a number of trials until the right CVs are found.

In protein folding, the number of degrees of freedom is enormously huge and the underlying topology of the systems is very complex. Thus, Metadynamics usually has been combined with REMD which was described before (e.g. bias-exchange Metadynamics). However, it should be noted that a sufficient overlap between the potential energy distributions of neighbouring replicas is needed and Metadynamics-REMD scales not optimal with increasing system size. The combination of REMD with the well-tempered ensemble (WTE) should also be mentioned here, which uses a bias potential depending on the time-dependent potential energy of the system [65]. Metadynamics has been applied successfully on folding of the GB1- hairpin [67, 68], and the effect of point mutations on the headpieces of Villin and Advillin [69]. This method has been applied to explore the conformation FEL of the prion protein [70], the dynamics of a kinase domain [71] and processes connected to proline isomerization [72]. We mention a study on folding of TrpCage, where multiple biases where applied on the system in form of a bias-exchange Metadynamics technique [47]. In another work, the bias potential is varied according to an associated variational approach for the determination of the folding free energy surface of small peptides [72]. Finally, we mention that as in the case of REMD a formalism has been proposed for the estimation of kinetics in Metadynamics [73].

1.3 HYBRID KINETIC MONTE CARLO - MD

The hybrid kinetic Monte Carlo (kMC) - MD method presented here, is a technique for the semi-deterministic propagation of a particle based protein system. It consists of sequential alternations of MD-phases and particle based kMC-steps. In kMC-MD, the kMC step performs transitions from one minimum along the FEL to another [78, 79]. For this structure-based transition within one specific kMC step, a priori assumptions have to be made on the rate determining processes the system can perform in general (see Figure 6). In terms of time-accuracy and the unrestrained access of the conformation space
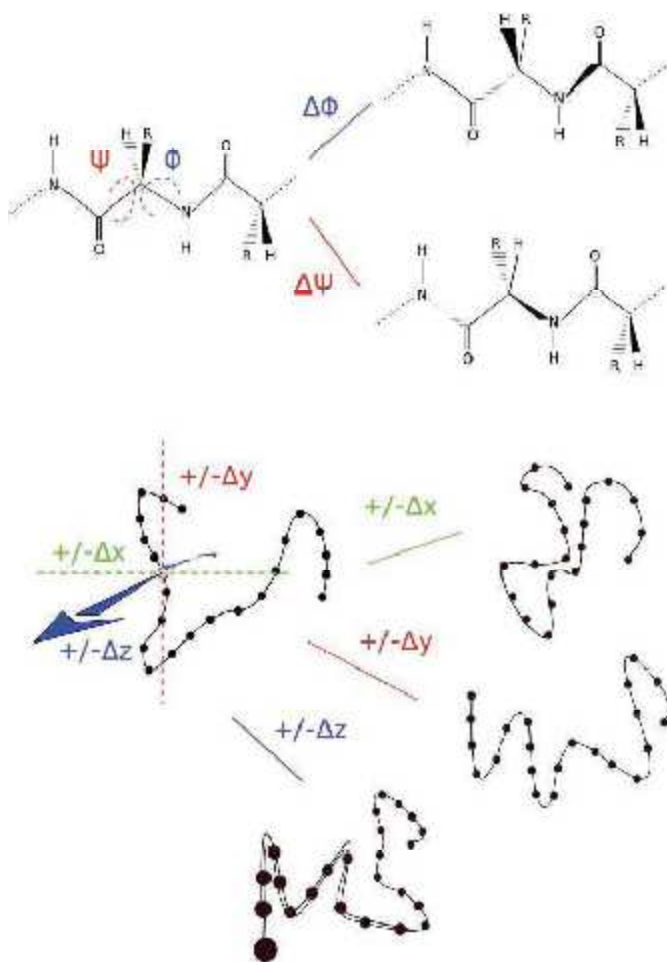
Fig. 6: Schematic description of kMC-moves used in the kMC-MD method. As described in the main text, the kMC moves used for the simulation of folding of peptides included dihedral rotations and longitudinal moves of segments in the polypeptide chain [74, 76].

of the protein, the set of all possible moves has to be sufficiently complete. For proteins, we have selected dihedral rotations and aminoacid translations as essential moves which are performed by individual aminoacids in the protein. Each of these kMC events is at first probed for its transition state energy through a stepwise transition in the dihedral angle or the H-bond distance of one aminoacid. For each step, after, e.g. the H-bonding distance or the dihedral angle has been changed, a thermodynamic integration step is performed in order to determine the free energy at one certain position along the one-dimensional reaction coordinate for this particular event. This very process is performed for a number of defined steps, and finally a list of transition energies is generated consisting of all events (H-bond moves, dihedral rotations) of the aminoacids of one selected group in the protein sequence. The rate r_i of each event is then calculated according to Kramer s rate description in the condensed phase [80, 81].

Initially, the kMC-MD method has been applied to the signaling dynamics of the light, oxygen or voltage sensitive domain 2 from *Avena sativa* (oat) (AsLOV2). AsLOV2 is part of the photosensory protein-complex phototropin1 (As-phot1) consisting of 2 domains and a C-terminal Ser-Thr kinase responsible for the phototropic response of the plant. AsLOV2 contains Flavin-Mo-

no-Nucleotide (FMN) as co-factor, which undergoes a photocycle after irradiation with blue-light (450 nm). This photocycle consists of the formation of a triplet state (lifetime ca. 4 µs) followed by covalent bond-formation with a reactive cysteine residue (Cys450). This signalling state persists for many seconds until AsLOV2 converts back to its dark state. The signalling behavior of AsLOV2 is connected to the time-scale problem, since the signalling dynamics occur on time-scales of seconds and longer. Therefore, we developed the kMC-MD methodology, in which the time-scales have been separated between the signalling dynamics within the Flavin-binding pocket and exterior parts of AsLOV2 [78]. The time-dependent events in the binding pocket of AsLOV2 could be described in agreement with MD-simulations, and the method described the late stages of the signalling state in agreement with experiments [82, 83].

In a subsequent study, we developed a fully residue based kMC-MD method, which performs residue-based kMC-moves along the whole protein sequence. Through this development, the separation of time-scales within the kMC-phase became negligible. In that way, large protein domains can be simulated with the kMC-MD method. We developed a model for full-length phototropin1 from *Chlamydomonas reinhardtii* consisting of 2 LOV-domains and a C-terminal kinase domain connected by inter-domain linker regions. We found that these linker regions play an essential role in signalling of phototropin1 in the signalling state. This linker region partially unfolds in the dark state, while the linker region forms a helix-turn-helix (HTH) motif in the signalling state [79]. These kMC-MD results were confirmed by later experiments [84].

Encouraged by this success, we developed and applied kMC-MD on protein folding problems. We validated this method on folding of TrpCage starting from a fully extended polypeptide chain (see Figure 7). We found that different kMC moves lead to different folding pathways (see Figure 8). Dihedral moves along the backbone combined with H-bond moves lead predominantly to a diffusion-collision pathway with a preferential formation of secondary structure. Longitudinal moves involving the formation of contacts along the tertiary structure lead to a preference of the nucleation condensation pathway of Trp-Cage with prior formation of the tertiary structure [74]. Due to the computational efficiency of the kMC-MD approach, we performed a total of 40 folding simulations. We observed that the folding time itself also strongly depends on the selected set of kMC moves. The complete move set described folding along both pathways, while the folding time was in the experimental range of 4 µs. Recently, we generalised the move sets for folding of β-stranded and α-helical peptides [76]. Here, we modified the longitudinal moves for tertiary structure formation to moves along Cartesian axes, and showed that this algorithm was able to fold reliably TrpCage, TrpZip4 and GB1 [76].

The kMC-MD formalism presented here is different from the approaches presented previously, since it accelerates the folding dynamics with no a priori criteria, e.g. selection of collective variables in Metadynamics or the selection of the temperature range in REMD. In kMC-MD, the dynamics are propagated by time-dependent steps, and can be described in dependency of kMC transition rates. The only external condition on the dynamics
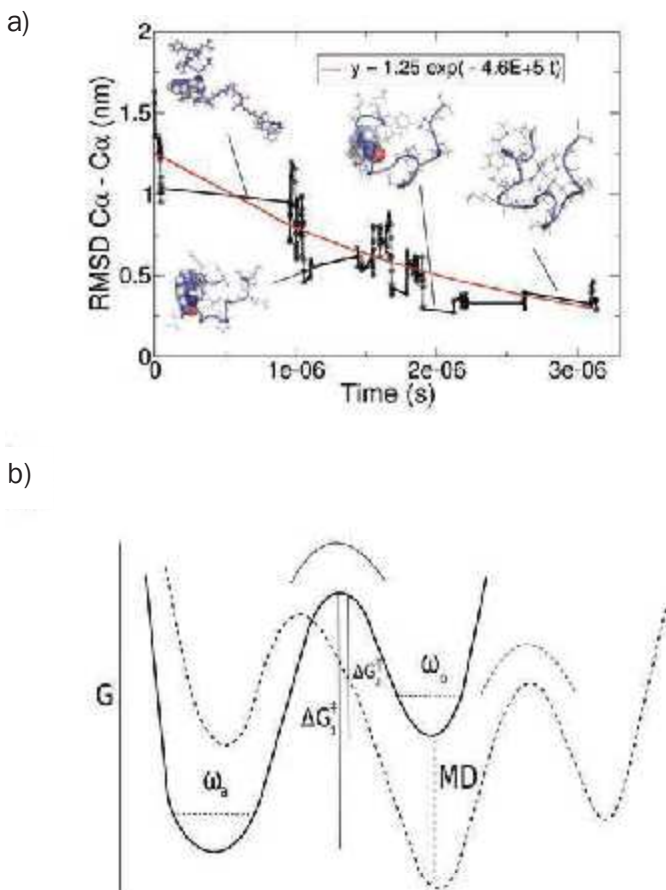
a)

b)

Fig. 7: (a) Root mean square deviation (RMSD) to the backbone of the native structure (PDB : 1L2Y [75]) as function of kMC-time [73]. The folding pathway occurs along a 2-state pathway, i.e. the time-dependent decay follows a mono-exponential function. The folding time and the 2-state behavior are in agreement with experiments [6]. (b) Schematic description of 2-dimensional free energy profiles in the course of a kMC-MD simulation. In each kMC-step, the system can change into another metastable minimum and can cross transition state barriers. In the subsequent MD-phase the system can propagate into the minimum of this state (Here, the minimum is located orthogonal to the reaction coordinate). In the next kMC-step, the system can propagate into another metastable state. In that way, kMC-MD enhances sampling in combination with a given time-information which is determined on the fly [78].

of the system are the assumptions on the move-sets, i.e. dihedral rotations, longitudinal moves etc. If this set of kMC-process paths is not complete, folding pathways and the free energy landscape are confined to certain regions depending on the selected processes. Each kMC-step is associated with a kMC-time, which is larger than the MD-timescale by one or two orders of magnitude. In that way, the kMC-MD method is based on a separation of time-scales between MD and kMC. As an alternative view, the kMC-step coarse-grains the fine-grained dynamics of MD and performs rare-event dynamics which would occur on a long timescale in MD. Thus, a kMC-MD simulation should in the ideal case converge to the un-biased (conventional) MD-trajectory of the same time-scale. We note that kMC-MD can speed up sampling of protein systems by a factor of 100-1000 at low computational cost, e.g. 3-5 days on a 8-core Desktop computer for one kMC-MD folding simulation, compared to 5 weeks using 320 cores on a supercomputer for a conventional REMD or a Bias-Exchange REMD simulation. In that way, we conclude that long time-scales can be reached in simulations of protein-folding at low computational cost with the possibility to exhaustively sample folding of proteins with a sufficiently large number of simulations.
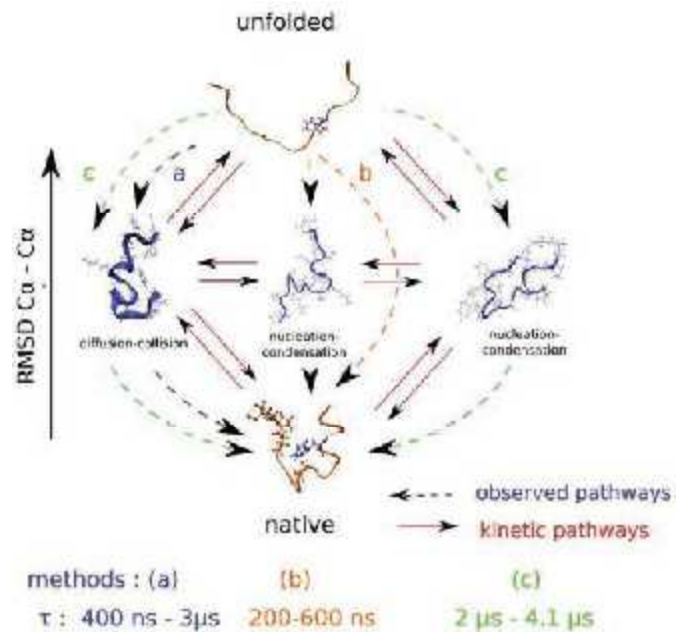

Fig. 8: Intermediates found in kMC-MD simulations of folding of the TrpCage miniprotein including the time-information and observed pathways. The latter depend on the applied kMC-moves: Method(a) considers only dihedral rotations and H-bond formation/breakage moves. Method(b) uses only moves which aim on the formation and breakage of contacts along the peptide chain. Method(c) uses the complete set of kMC-moves. While the kMC-MD simulation, which employs secondary structure moves follows a diffusion collision pathway, tertiary structure moves lead to a preference for the nucleation condensation pathway of folding. A combination of both move-sets facilitates both pathways.

1.4 CONCLUSIONS

In this article, we presented and compared 3 different enhanced sampling methods for the simulation of protein folding. We started with replica exchange MD which enhances sampling through the simulation in parallel ensembles at different temperatures and frequent swapping in temperature space. Various improvements in REMD have been developed, which aim on a decrease of the needed amount of replicas while the temperature differences can be increased. Metadynamics is a method based on the definition of fundamental collective variables, which describe reaction coordinates in the system. These collective variables define the space of the time-dependent bias potential, which is subsequently filled with Gaussians throughout the simulation. Thereby, the system can escape from free energy minima and is prevented to revisit states. Finally, we presented a new development based on a hybridisation of kinetic-Monte Carlo and MD (kMC-MD). This method is based on a separation of timescales between the kMC- and the MD-phase. While the MD-phase relaxes the structure of the polypeptide within its thermodynamic state, the kMC phase crosses long timescales through a structural transition connected to a rate-dependent time. In a recent development, the peptide can transition from one state to another by a sequence of dihedral rotations and translations. It has been shown that the new algorithm is able to fold reliably α-helical and β-stranded peptides. We emphasise that the computational cost of kMC-MD is low, while long time-scales can be reached with this new technique and the kinetics are in agreement with experimental data.

1.5 ACKNOWLEDGEMENTS

REFERENCES

[1] V. Cherezov, D. M. Rosenbaum, M. A. Hanson, S. G. F. Rasmussen, F. S. Thian, T. S. Kobilka, H. J. Choi, P. Kuhn, W. I. Weis, B. K. Kobilka, R. C. Stevens, *Science,* **318**, 1258-1265 (2007).

[2] H. M. Berman, J. Westbrook, Z. Feng, G. Gilliland, T. N. Bhat, H. Weissig, I. N. Shindyalov, P. E. Bourne, *Nucleic Acids Res.,* **28**, 235-242 (2000).

[3] C. Nilsberth, A. Westlind-Danielsson, C. B. Eckmann, M. M. Condron, K. Axelman, C. Forsell, C. Stenh, J. Luthman, D. B. Teplow, S. G. Younkin, J. Naeslund, L. Lannfeld, *Nat. Neurosci.,* **4**, 887-893 (2001).

[4] J. Kubelka, J. Hofrichter, W. A. Eaton, *Curr. Opin. Struct. Biol.,* **14**, 76 88 (2004).

[5] C. Levinthal, *J. Chim. Phys. Phys. Chim. Biol.,* **65**, 44 45 (1968).

[6] J. N. Onuchic and P. G. Wolynes, *Curr. Opin. Struct. Biol.,* **14**, 70 75, (2004).

[7] L. Qiu, S. A. Pabit, A. E. Roitberg, S. J. Hagen., *J. Am. Chem. Soc.,* **124**, 12952 12953 (2002).

[8] M. M. Babu, R. van der Lee, N. S. de Groot, J. Gsponer., *Curr. Opin. Struct. Biol.,* **21**, 432 440 (2011).

[9] J. Martin, F. U. Hartl, *Curr. Opin. Struct. Biol.,* **7**, 41 52 (1997).

[10] R. S. Spolar, J.-H. Ha, M. T. Record Jr., *Proc. Natl. Acad. Sci. U.S.A.,* **86**, 8382 8385 (1989).

[11] P. L. Freddolino, C. B. Harrison, Y. Liu, K. Schulten, *Nat. Phys.,* **6,** 751 758 (2010).

[12] J. E. Shea and C. L. Brooks, *Curr. Opin. Struct. Biol.* **52** 499-535 (2001).

[13] P. L. Freddolino, F. Liu, M. Gruebele, and K. Schulten, *Biophys. J.,* **94**, 75 77 (2008).

[14] D. E. Shaw, P. Maragakis, K. Lindorff-Larsen, S. Piana, R. O. Dror, M. P. Eastwood, J. A. Bank, J. K. S. J. M. Jumper, and W. W. Y. Shan, *Science,* **15**, 341 346 (2010).

[15] A. F. Voter, F. Montalenti, and T. C. Germann, *Annu. Rev. Mater. Res.,* **32**, 321 346 (2002).

[16] K. Hukushima and K. Nemoto, *J. Phys. Soc. Jpn.,* **65**, 1604 1608, 1996.

[17] T. Okabe, M. Kawata, Y. Okamoto, and M. Mikami, *Chem. Phys. Lett.,* **335**, 435 439, 2001.

[18] W. Zhang, C. Wu, and Y. Duan, *J. Chem. Phys.,* **123**, 154105, 2005.

[19] J. Juraszek and P. G. Bolhuis, *Proc. Natl. Acad. Sci. U.S.A.,* **103**, 15859 15864, 2006.

[20] J. Zhang and J. S. Liu, *PLoS Comput. Biol.,* **2**, e168, 2006.

[21] Y. M. Rhee and V. S. Pande, *Biophys. J.,* **84**, 775 786, 2003.

[22] C. Bergonzo, N. M. Hendriksen, D. R. Roe, J. M. Swails, A. E. Roitberg, and T. E. C. III, *J. Chem. Theor. Comput.,* **10**, 492 499, 2013.

[23] C. Chen, Y. Xiao, and Y. Huang, *Phys. Rev. E,* **91**, 052708, 2015.

[24] J. M. Swails, D. M. York, and A. E. Roitberg, *J. Chem. Theor. Comput.,* **10**, 1341 1352, 2014.

[25] W. Jiang and B. Roux, *J. Chem. Theor. Comput.,* **6**, 2559 2565, 2010.

[26] J. Hritz and C. Oostenbrink, *J. Chem. Phys.,* **128**, 144121, 2008.

[27] J. Kim, J. E. Straub, and T. Keyes, *J. Phys. Chem. B,* **116**, 8646 8653, 2012.

[28] Y. Sugita and Y. Okamoto, *Chem. Phys. Lett.,* **329**, 261 270, 2000. A. Mitsutake, Y. Sugita, and Y. Okamoto, *J. Chem. Phys.,* **118**, 6664, 2003.

[29] Mitsutake, Y. Sugita, and Y. Okamoto, *J. Chem. Phys.,* **118**, 6676, 2003.

[30] F. Calvo and J. P. K. Doyle, *Phys. Rev. E,* **63**, 010902, 2000.

[31] R. Faller, Q. Yan, and J. J. de Pablo, *J. Chem. Phys.,* **116**, 5419, 2002.

[32] T. W. Whitfield, L. Bu, and J. E. Straub, *Physica A,* **305**, 157 171, 2002.

[33] S. Jang, S. Shin, and Y. Pak, *Phys. Rev. Lett.,* **91**, 058305, 2003.

[34] P. Liu, B. Kim, R. A. Friesner, and B. J. Berne, *Proc. Natl. Acad. Sci. U.S.A.,* **102**, 13749 13754, 2005.

[35] P. Liu, X. Huang, R. Zhou, and B. J. Berne, *J. Phys. Chem. B,* **110**, 19018 19022, 2006.

[36] X. Cheng, G. Cui, V. Hornak, and C. Simmerling, *J. Phys. Chem. B,* **109**, 8220 8230, 2005.

[37] E. Lyman, M. Ytreberg, and D. M. Zuckerman, *Phys. Rev. Lett.,* **96**, 028105, 2006.

[38] P. Liu and G. A. Voth, *J. Chem. Phys.,* **126**, 045106, 2007.

[39] F. Calvo, *J. Chem. Phys.,* **123**, 124106, 2005.

[40] S. W. Rick, *J. Chem. Phys.,* **126**, 054102, 2007.

[41] H. Kamberaj and A. van der Vaart, *J. Chem. Phys.,* **127**, 234102, 2007.

[42] P. Brenner, C. R. Sweet, D. VonHandorf, and J. A. Izaguirre, *J. Chem. Phys.,* **126**, 074103, 2007.

[43] C. Zhang and J. Ma, *Phys. Rev. E,* **76**, 036708, 2007.

[44] S. Trebst, M. Troyer, and U. H. E. Hansmann, *J. Chem. Phys.,* **124**, 174903, 2006.

[45] J. Ballard and C. Jarzynski, *Proc. Natl. Acad. Sci. U.S.A.,* **106**, 12224 12229, 2009.

[46] P. Kar, W. Nadler, and U. H. Hansmann, *Phys. Rev. E,* **80**, 056703, 2009.

[47] F. Marinelli, F. Pietrucci, A. Laio, and S. Piana, *PLOS Comput. Biol.,* **5**, e1000452, 2009.

[48] R. Zhou, *Proc. Natl. Acad. Sci. U.S.A,* **100**, 13280 13285, 2003.

[49] Y. Xiao, C. Chen, and Y. He, *Int. J. Mol. Sci.*, **10**, 2838 2848, 2009.

[50] D. D. Sancho, J. Mittal, and R. B. Best, *J. Chem. Theor. Comput.*, **9**, 1743 1753, 2013.

[51] D. Paschek, S. Hempel, and A. E. Garcia, *Proc. Natl. Acad. Sci. U.S.A.*, **105**, 17754 17759, 2008.

[52] D. Paschek, R. Dayb, and A. E. Garcia, P*hys. Chem. Chem. Phys.*, **13**, 19840 19847, 2011.

[53] E. K. Peter, M. Agarwal, B. Kim, I. V. Pivkin, and J.-E. Shea, *J. Chem. Phys.*, **141**, 22D511, 2014.

[54] Bhattacharya, R. B. Best, and J. Mittal, *Biophys. J.*, **103**, 596 600, 2012.

[55] C. Wu and J.-E. Shea, *Curr. Opin. Struct. Biol.*, **21**, 209 220, 2011.

[56] G. M. Torrie and J. P. Valleau, *J. Comput. Phys.*, **23**, 187 199, 1977.

[57] T. Huber, A. E. Torda, and W. F. Gunsteren, *J. Comput.-Aided Mol. Des.*, **8**, 695 708, 1994.

[58] H. Grubmueller, *Phys. Rev. E*, **52**, 2893 2906, 1995.

[59] E. M. Mueller, A. de Meijere, and H. Grubmueller, *J. Chem. Phys.*, **116**, 897 905, 2002.

[60] E. Darve and A. Pohorille, *J. Chem. Phys.*, **115**, 9169 9183, 2001.

[61] K. Park and K. Schulten, *J. Chem. Phys.*, **120**, 5946 5961, 2004.

[62] S. Marsili, A. Barducci, R. Chelli, P. Procacci, and V. Schettino, *J. Phys. Chem. B*, **110**, 14011 14013, 2006.

[63] M. Iannuzzi, A. Laio, and M. Parrinello, *Phys. Rev. Lett.*, **90**, 238302, 2003.

[64] Laio, A. Fortea-Rodriguez, F. Gervasio, M. Ceccarelli, and M. Parrinello, *J. Phys. Chem. B*, **109**, 6714 6721, 2005.

[65] M. Bonomi and M. Parrinello, *Phys. Rev. Lett.*, **104**, 190601, 2010.

[66] M. Bonomi, D. Branduardi, F. L. Gervasio, and M. Parrinello, *J. Am. Chem. Soc.*, **130**, 13938 13944, 2008.

[67] G. Bussi, F. L. Gervasio, A. Laio, and M. Parrinello, *J. Am. Chem. Soc.*, **128**, 13435 13441, 2006.

[68] S. Piana, A. Laio, F. Marinelli, M. V. Troys, D. Bourry, C. Ampe, and J. C. Martins, *J. Mol. Biol.*, **375**, 460 470, 2008.

[69] A. Barducci, R. Chelli, P. Procacci, V. Schettino, F. L. Gervasio, and M. Parrinello, *J. Am. Chem. Soc.*, **128**, 2705 2710, 2006.

[70] A. Barducci, A. Cavalli, D. Branduardi, F. L. Gervasio, M. Recanatini and M. Parrinello, *J. Am. Chem. Soc.*, **130**, 13938 13944, 2009.

[71] C. Melis, G. Bussi, S. C. R. Lummis, and C. Molteni, *J. Phys. Chem. B*, **113**, 12148 12153, 2009.

[72] O. Valsson and M. Parrinello, *Phys. Rev. Lett.*, **113**, 090601, 2014.

[73] P. Tiwary and M. Parrinello, *Phys. Rev. Lett.*, **111**, 230602, 2013.

[74] E. K. Peter and J.-E. Shea, *Phys. Chem. Chem. Phys.*, **16**, 6330 6340, 2014.

[75] J. W. Neidigh and R. M. Fesinmeyer, *Nat. Struct. Biol.*, **9**, 425 430, 2002.

[76] E. K. Peter, I. V. Pivkin, and J.-E. Shea, *J. Chem. Phys.*, **142**, 144903, 2015.

[77] L. Qiu, S. A. Pabit, A. E. Roitberg, and S. J. Hagen, *J. Am. Chem. Soc.*, **124**, 12952 12953, 2002.

[78] E. Peter, B. Dick, and S. A. Baeurle, *J. Chem. Phys.*, **136**, 124112, 2012.

[79] E. K. Peter, B. Dick, I. Stambolic, and S. A. Baeurle, *Proteins*, **81**, 394, 2014.

[80] H. A. Kramers, *Physica (Utrecht)*, **7**, 284, 1940.

[81] P. Haenggi, P. Talkner, and M. Borkovec, *Rev. Modern Phys.*, **62**, 251 332, 1990.

[82] S. M. Harper, L. C. Neil, and K. H. Gardner, *Science*, **301**, 1541 1544, 2003.

[83] E. Peter, B. Dick, and S. A. Baeurle, *Nat. Commun.*, **1**, 122, 2010.

[84] Y. Nakasone, Y. Kawaguchi, S.-G. Kong, M. Wada, and M. Terazima, *J. Phys. Chem. B,* **118**, 14314 14325, 2014.

Stefanie Tschierlei and Nils Rockstroh

ELECTRON TRANSFER PROCESSES IN INTER- AND INTRAMOLECULAR SYSTEMS FOR PHOTOCATALYTIC HYDROGEN EVOLUTION

KEYWORDS

hydrogen, intra- and intermolecular electron transfer, Raman spectroscopy, time-resolved transient absorption spectroscopy, catalytic intermediates.

INTRODUCTION

Hydrogen is considered as a key component in future energy systems due to its ability of energy storage, which would mitigate current problems of intermittent availability of renewable energies.[1, 2] Current research uses several approaches to obtain hydrogen from renewable sources such as electrolysis of water by wind energy or photocatalytic water splitting. In the latter case natural photosynthesis serves as the blueprint. In brief, absorption of light in two spatially separated photosystems (photosystem I and II) provides the energy for water oxidation and NADPH formation.[3] This separation was adopted by different research labs focusing either on proton reduction or water oxidation using sacrificial agents. By doing so, basic processes of electron and/or proton transfer could be easier examined. This strategy will contribute to deepen the understanding of the underlying mechanisms, which is crucial for the development of integrated solar water splitting devices.

The main subject of this contribution is the presentation of different methods and mechanistic investigations of systems, which are able to undergo the reduction half-reaction resulting in hydrogen evolution. One approach comprises the development and analysis of heterogeneous materials like oxide and sulfide semiconductor composites, e.g. titania, polymer-based semiconductor composites[4] and also combinations thereof with molecular complexes. A thorough overview on these materials can be found in a recent review of Marschall.[5]

Another possibility to enable water reduction with visible light is the utilization of molecular systems like in natural photosynthesis. In these systems a light harvesting unit, the so-called photocenter or photosensitizer, is required. Metal complexes of e.g. Ru, Os and Ir are prominent examples of molecular photosensitizers, where visible light absorption is enabled by a long-lived metal-to-ligand-charge-transfer (MLCT).[6, 7] In dyads this photo subunit is directly connected via a bridging ligand to a second metal, which acts as catalytic center, where the reduction reaction occurs (Fig. 1, top). To recover the photocatalyst and to close the catalytic cycle sacrificial reagents are required. Recent advances in the development of such (supra-)molecular devices, where the whole reaction occurs within one molecule, have been reported.[8] The advantages of such intramolecular systems are obvious: a) modular construction, b) direct influence on catalytic and photophysical properties through changes of the structure, c) fast light-induced intramolecular electron transfer processes from the photocenter to the catalytic center and d) a directional electron transfer minimizing loss of energy which is tunable by the choice of the substituents. These all-in-one systems offer the chance to analyze the underlying structure-activity-properties in detail. Since the electron transfer processes are very fast, femtosecond transient absorption spectroscopy is a suitable method.
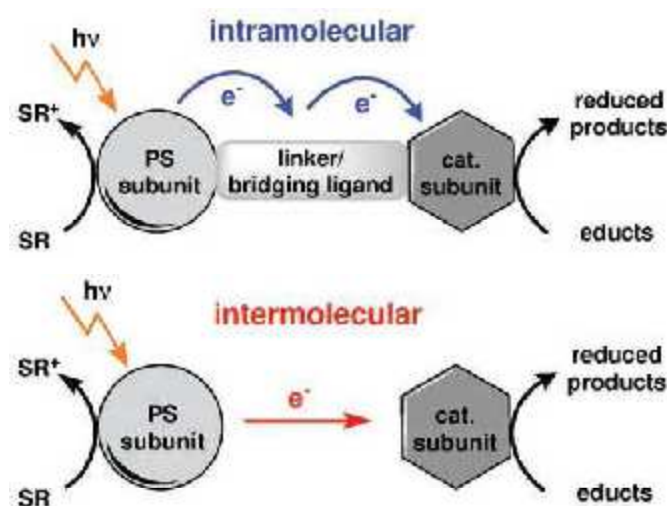

Fig. 1: Representation of the different steps during the photocatalytic reactions within an intra- (top) and an intermolecular system (bottom). After light harvesting with a photocenter (PS, photosensitizer) an electron is transferred to the catalytic center (cat. subunit), where the reduction reaction takes place. A sacrificial reagent (SR) recovers the PS.

Dr. Stefanie Tschierlei
Institute of Organic Chemistry, University of Stuttgart
Pfaffenwaldring 55, 70569 Stuttgart, Germany
E-Mail: stefanie.tschierlei@oc.uni-stuttgart.de

Dr. Nils Rockstroh
Leibniz Institute for Catalysis at the University of Rostock (LIKAT)
Albert-Einstein-Str. 29a, 18059 Rostock, Germany
E-Mail: nils.rockstroh@catalysis.de

Another molecular approach, closer to the concept of the photosynthesis, is the usage of different small and convenient molecules fulfilling the various tasks during the reduction reaction separately. In this case, the photocenter is most often a coordination compound based on ruthenium,[6] iridium[7] or even copper.[9] Contrary to dyads, no direct connection to the catalytic center exists, and thus, the catalyst can be changed independently over a wide range. Mostly, cobalt catalysts[10] or mimics of the active sites of natural hydrogenase enzymes (iron systems),[11, 12] which can fulfill the reversible proton reduction or hydrogen oxidation, are used. The essential electron transfer processes from the photosensitizer to the catalytic subunit take only place by the direct interaction of the different molecules via collision. These processes are much slower compared to the transfer of the first electron in intramolecular approaches and occur in the nano- to microsecond time scale. Moreover, the light-induced intermediates appearing during the intermolecular catalytic processes are easier to identify by nanosecond transient absorption spectroscopy, because a comparison with the spectroscopic features of the reduced and/or protonated species by means of UV/vis or FTIR spectro-electrochemistry is accessible.

INTRAMOLECULAR PROCESSES   FIRST STEP

Molecular photocatalysts, which combine the photo unit with a catalytic unit via a bridge, have attracted a lot of attention in the last decades.[8] One research focus is dedicated to the bridge, because a directed electron transfer between the active parts as well as the storage of electrons is feasible for further catalytic steps. Besides, such combined systems offer the opportunity to intensively study the correlation between the electron transfer steps and the catalytic results, the so-called structure-activity-relationships. One prominent example of a hydrogen evolving complex is [(tbbpy)Ru(tpphz)PdCl$_2$]$^{2+}$ (**RuPd** with tbbby = 4,4 -di-*tert*-butyl-2,2 -bipyridine and tpphz = tetrapyrido[3,2-a:2 ,3 -c:3 ,2 -h:2 ,3 -j]phenazine, see inset Fig. 2).[13]

For **RuPd** the turnover number (TON), which is the produced amount of hydrogen per mole of catalyst, has been analyzed in dependence on the excitation wavelength.[13] The highest hydrogen yield was obtained with blue light of 458 nm and the TON is decreased by the usage of increasing wavelengths (more red light). In contrast to the slope of the respective absorption spectrum (black line Fig. 2, bottom) the decline of the TON is weaker. Consequently, the catalytic efficiency, which is obtained by division of TON by ε, depends on the color of the photons and increases with larger wavelengths as depicted in Fig. 2, bottom (circles). After absorption these photons induce a metal-to-ligand charge transfer from Ru to the coordinated ligands raising the question of a correlation between catalytic efficiency and the features of this first step of the photocatalytic process. In particular, the elucidation of the localization of the excited states on the ligands was in the center of attention, which could be ideally investigated with resonance Raman spectroscopy. Using this approach information about modes with a large displacement from the equilibrium geometry at the Frank-Condon point could be obtained, which provides direct evidence for the localization of the excited state (resulting in enlarged Raman
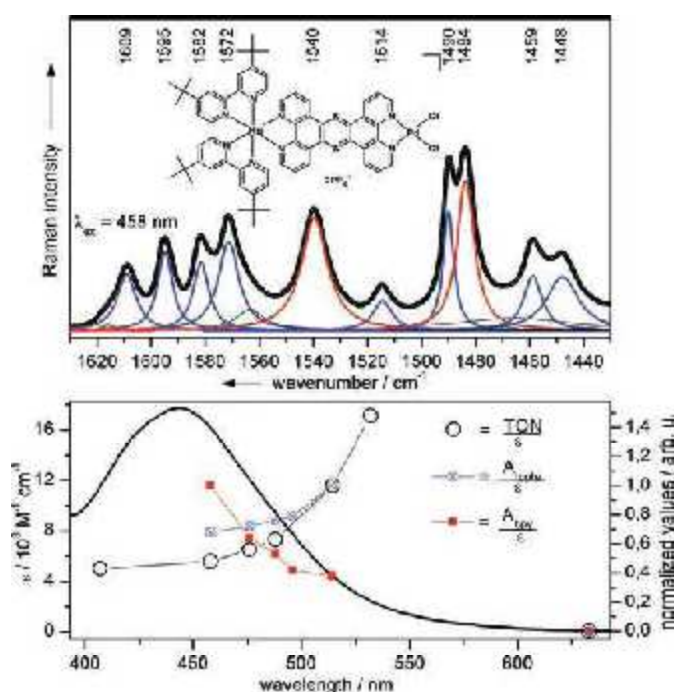

Fig. 2: Top: Structure of RuPd. Resonance Raman Spectrum (black) of RuPd excited at 458 nm. The Raman bands were quantitatively analyzed by deconvolution with Lorentzian profiles. Assignment to the terminal tbbpy ligand (red) and bridging tpphz ligand (blue). Bottom: Absorption spectrum of RuPd in acetonitrile (black line), normalized efficiency spectrum of the hydrogen catalysis is the division of TON by the extinction coefficient ε (circles), normalized Raman band areas A divided by extinction coefficient ε of RuPd of tbbpy (blue crosses) and tpphz ligand (red rectangles) at different excitation wavelengths. The values of the catalytic efficiency and the areas are normalized to 458 nm.

bands).[15] With an excitation wavelength of 458 nm the analysis of the Raman spectrum (Fig. 2, top, black) reveals that both ligands, the terminal tbbpy (red) and the tpphz bridge (blue), are involved in the underlying metal-to-ligand charge transfer (MLCT) transitions. Quantitative analysis of the assigned Raman bands at different excitation wavelengths discloses different areas for both ligands. The ratio of the area of the Raman bands of the bridging ligand tpphz to the total area of the whole Raman spectrum increases with increasing wavelength, which means that the area per extinction increases as well (Fig. 2, bottom blue and red). Thus, the electron density of the excited state shifts from the terminal to the bridging ligand if the used photons are redder. This experimental result of the Raman spectroscopy was also confirmed by extended time-dependent DFT calculations. Moreover, the comparison of these findings shows an obvious correlation between the localization of the excited state at the tpphz ligand and the hydrogen amount.[14]

In conclusion, the importance of the initial photoexcitation for the efficiency of catalysis is emphasized. Notably, a MLCT to the terminal tbbpy ligands results in a less pronounced contribution to hydrogen evolution and the direct involvement of the bridge is favorable. Thus, not only the capability of the bridge to store electrons for the catalytic process, but also the initial photoexcitation steps are crucial and should be considered for the design of new all-in-one photocatalysts. An optimal design hampers the contribution of the terminal ligand(s) and pushes the electron transfer through the photoexcitation straight toward the intramolecularly linked catalytic center.

INTRAMOLECULAR PROCESSES   ELECTRON TRANSFER STEPS

Depending on the excitation wavelength the MLCT transitions are spread over the different ligands of **RuPd** (see section above). However, from resonance Raman spectra only information about the first 20 fs after photoexcitation are known. For the overall catalysis the subsequent processes are also of high interest. Only the knowledge about the pathways, the steps and the required times enables a further improvement of such intramolecular photocatalysts. To gain information transient absorption spectroscopy with femtosecond time resolution is appropriate.

To analyze the spectral signatures it is convenient to characterize the mononuclear complex $[(tbbpy)Ru(tpphz)]^{2+}$ (**Ru**) without any catalytic unit to get a clue about the underlying processes. As a result, the obtained pump-probe data in acetonitrile with an excitation wavelength of 507 nm could be fitted with two time constants, τ_1 = 1.2 ps and τ_2 = 240 ps.[16] The first time constant could be explained with the formation of a phenanthroline centered ^{3}MLCT state after the initial population of tpphz and tbbpy, which is also known as interligand hopping from the terminal tbbpy to the bridging tpphz ligand. Afterwards, this phenanthroline based excited state is depopulated within 240 ps and simultaneously a long-lived excited state is populated, which is localized on the phenazine part of the tpphz (Fig. 3, time constants in brackets). Finally, the deactivation of this long-lived state occurs as emission and takes place in 154 ns in air-saturated acetonitrile.[13]
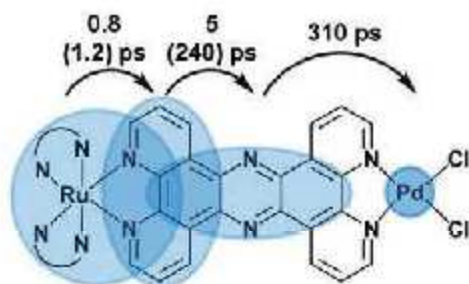

Fig. 3: Photoinduced electron transfer from the photo-center to the catalytic center. The time constants for RuPd and Ru (in brackets) have been obtained by femtosecond time-resolved transient absorption spectroscopy in acetonitrile.[16]

The initial MLCT transitions in **RuPd** are not affected by the coordination of a PdCl$_2$ unit on the tpphz ligand and are still spread over the three coordinating ligands. However, the driving force of the subsequent electron transfer processes is increased and the interligand hopping occurs in 0.8 ps and the population of the phenazine sphere of the tpphz is followed in 5 ps (Fig. 3). Especially the latter transition is almost two orders of magnitude faster compared to the situation in **Ru**. In the case of **Ru** this populated excited state lives nanoseconds, but for **RuPd** the state decays within 310 ps and no comparable feature could be detected in **Ru**. Thus, this process was assigned in accordance to the literature to a ligand-to-metal charge transfer from the tpphz moiety to the Pd unit.

In conclusion, femtosecond time-resolved transient absorption spectroscopy provided insights into the fast electron transfer processes of an intramolecularly working photocatalyst. It was shown that the first light-induced reduction of the Pd(II) ion, which acts as the catalytic center, occurs in less than 310 ps in a polar solvent.

Hence, the first electron of the catalysis is not stored at the bridging ligand and is instead directly transferred to Pd. Thus, this electron transfer is much faster than the recovery of the photocatalyst by the sacrificial donor, because this regeneration is diffusion limited and much slower (nano- to microsecond time scale). It is also clear that the first electron is not the rate limiting step of the catalytic hydrogen production. Therefore, the focus of future work should lie on the stabilization of the catalytically active species[17, 18] and on the detection of the pathways of the second electron,[19] which is necessary to accomplish the proton reduction.

One approach towards this goal comprises the use of a bridging ligand with an extended π-system, e.g. tri(phenanthrolino) hexaazatriphenylene (phat). This ligand allows the coordination of three metal centers, and thus, might combine two photocenters and one catalytic unit. However, catalysis did not work using this system, which shows the importance of the simultaneous presence of several factors such as sufficient electron transfer, availability of a second electron and sufficient reduction potentials.[20]

Another strategy to allow directed electron transfer comprises the supramolecular assembly of photosensitizer and catalyst via hydrogen bonds. Ligands bearing H donor functions, such as biimidazoles, offer a good opportunity to interact with H bond acceptors like polyoxometalates (POMs). Therefore, ruthenium biimidazole and bibenzimidazole complexes were reacted with $[\beta\text{-}Mo_8O_{26}]^{4-}$. Using biimidazole a 1:1 aggregate could be observed by X-ray crystallography. However, in the case of bibenzimidazole a rearrangement of the photosensitizer as well as the POM could be observed using nuclear magnetic resonance (NMR) spectroscopy, mass spectrometry (MS), electron absorption spectroscopy (UV/vis), X-ray and pH measurements. Thus, a transformation of the POM to $[Mo_6O_{19}]^{2-}$ and of the photosensitizer to a bridged dimer occurs. This process is mainly explained by the instability of the POM cluster, which could be confirmed by using a more stable one by phenylphosphonate substitution. This cluster formed again stable 1:1 aggregates with the photosensitizer.[21]

However, besides the initial photoexcitation and the subsequent electron transfer steps the stability is crucial. Therefore, intermolecular systems offer the great advantage of independent optimization with respect to electron transfer AND stability.

INTERMOLECULAR PROCESSES   THE PHOTOSENSITIZER UNIT

The intermolecular approach allows a very flexible handling, because the kind and the amount of the photo unit as well as the catalytic unit can be adjusted independently. Furthermore, the ratio of these components can be changed during the course of catalysis, which is an important advantage compared to supramolecular working systems, especially in the case of malfunction of one unit.

Besides the common use of Ru(II)[6] and Ir(III)[7] complexes also Cu(I) photosensitizers (CuPS) can be used as light harvesting

unit.[22,23] A new type of heteroleptic [Cu(P^P)(N^N)]+ complexes (**HET**), based on a sterically demanding diphosphine P^P and a diimine N^N ligand, has been designed and successfully used in terms of proton reduction. So far, with these **HET** complexes turnover numbers of more than 1000 hydrogen atoms per Cu complex[24] can be obtained compared to below 100 with homoleptic [Cu(N^N)$_2$]+ complexes (**HOM**).[25] Due to this large difference between these related CuPS it is of very high importance to understand the underlying structure-activity-relationships to be able to improve these photosensitizers.

A starting point is the analysis of the ground state structure of **HET-1** (Fig. 4, left) obtained by X-Ray crystallography. The geometrical arrangement of the PPNN atoms around the central Cu center is nearly tetrahedral, because the planes of the xantphos and the phenanthroline ligand form an angle of 83.8°.[26] In contrast to the substituted phenanthroline ligand in **HOM-1** (Fig. 4, right) the xantphos ligand is sterically more demanding and its backbone is distorted out of the plane. Thus, distortion of **HET-1** after photoexcitation is prevented by this phosphine ligand in combination with the substituents at the 2,9-position of the phenanthroline ligand (detailed description below). The results of this weaker flattening is: a) the emission maximum is shifted from 770 (**HOM-1**) to 569 nm (**HET-1**), b) the quantum yield is above 8 % and c) the emission lifetime is increased from some ns (**HOM-1**) to 6.4 µs (**HET-1**) in tetrahydrofuran.[27] Especially the very long emission lifetime for most **HET** in comparison to **HOM** indicates that the nucleophilic attack of the solvent molecules to the excited state, and consequently, the exciplex quenching is hindered.[27]
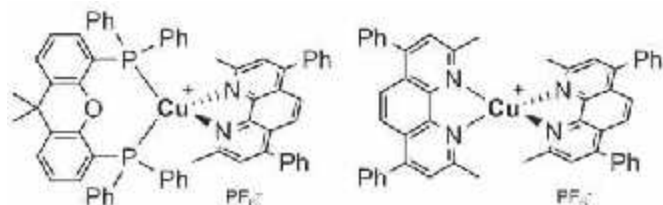

Fig. 4: Structure of HET-1 (left) and of the related HOM-1 (right).

A long lifetime of an excited state can be beneficial for a catalytic process, because the excited photosensitizer has much more time to interact with an electron donor or the catalyst.

Besides the different behavior of the triplet excited state of homoleptic and heteroleptic copper complexes it is also of interest to investigate the occurring processes directly after photoexcitation. For CuPS it is known that the metal-to-ligand charge transfer (MLCT) changes the formal electron configuration of the central copper ion from d^{10} to d^9. Subsequently, the ligand sphere responds to this change of the electron configuration by a geometrical reorganization from a tetrahedral to a distorted square-planar structure of the NNNN atoms around the metal center. This occurs within approx. 700 fs, followed by an intersystem crossing from the singlet to the respective triplet state, which is reached within 10 ps.[28]

The first surprising issue concerning photoexcitation of **HET-1** is the exclusive involvement of the diimine ligand in the MLCT process. In consequence, the extinction coefficient is only half as intense as in bisdiimine complexes and the changed electron density at the copper ion causes a hypsochromic shift in the absorption resulting in a yellow color (**HET**) of the complexes instead of red (**HOM**).

Based on this knowledge different heteroleptic Cu(I) complexes, selectively substituted at the 2,9-position of the phenanthroline with Me or n-Bu and at the 5,6-position with H or SO$_3$Na, were investigated by means of time-resolved femtosecond transient absorption spectroscopy. A summary of the occuring processes is depicted in Fig. 5. First, the distortion process could be detected, which is slower (1.0 ps for H and 1.4 ps for SO$_3$Na) compared to the time constants obtained for **HOM** (0.7 ps).[26, 28] On the one hand the steric diphosphine slows this process down and on the other hand the high molecular weight of the substituents at the diimine ligand seems to be relevant due to its influence on the force constants and inertia. The second step, the intersystem crossing from the singlet to the triplet state, is a bit faster compared to processes in **HOM** and occurs between 6.5 and 8.4 ps. Here, the electron-withdrawing group (SO$_3$Na) accelerates the process and the electron-donating group decreases the time constant. However, the ultrafast processes can be directly tuned by the substituents, but all in all the time constants are comparable to those obtained for **HOM**. Hence, the tuning possibilities by changing the ligands (phosphine instead of diimine) or the impact of substituent pattern is negligible for these ultrafast processes.
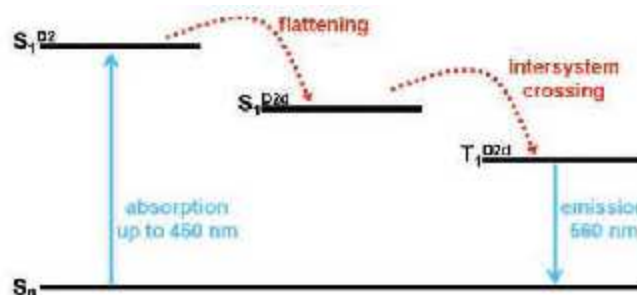

Fig. 5: Jablonski diagram of the excited state charge transfer processes in Cu(I) complexes after photoexcitation. Ground state (S$_0$), singlet excited state with D$_2$ symmetry (S$_1$D$_2$), singlet excited state with distorted D$_{2d}$ symmetry after the distortion of the ligand sphere (S$_1$D$_{2d}$), triplet excited state with D$_{2d}$ symmetry (T$_1$D$_{2d}$). The given point groups are assigned with respect to the surrounding geometry of a homoleptic copper center. However, the presence of P^P in HET leads to a decrease in symmetry (i.e. C$_{2v}$ instead of D$_2$).

In fact, it is appreciable to know that these processes are comparable for the different Cu(I) complexes, but all these steps are very fast and not rate liming in terms of photocatalysis and hydrogen production.

Based on this knowledge analysis of the further reaction steps to transfer one electron from the excited CuPS to the catalyst shall be undertaken. In principle, the photosensitizer can directly transfer one electron to the catalyst, which is called oxidative transfer, or can be reduced initially by a sacrificial electron donor and will donate the electron in a second step to the catalyst (Fig. 6, bottom). Cyclic voltammetry measurements revealed the reversibility of the reduction of **HET-1** and in combination with UV/vis and EPR spectroscopy the respective reduced intermediate could be detected (Fig. 6, top, blue).[29] Further, **HET-1** was reduced photochemically with triethylamine under visible light irradiation (Fig. 6, top, black). The obtained EPR signature was the same like the one observed during electrochemical treatment,[30] and thus, it is obvious that the photo-induced reduction is a possible pathway to transfer an electron to the catalyst. The same procedure was performed for the oxidative quenching mechanism with the result that the oxidized CuPS

can be obtained as well. Furthermore, a condition-dependent equilibrium between **HOM**, **HET** and $[Cu(P^\wedge P)_2]^+$ could be observed in solution,[31] which on the one hand presents a bottleneck due to a lack of stability and on the other hand allows for re-assembly of the active complex after ligand loss. However, despite the lack in stability the **HET**s are still necessary to successfully obtain hydrogen, because no catalytic activity is observed in the presence of **HOM** only.
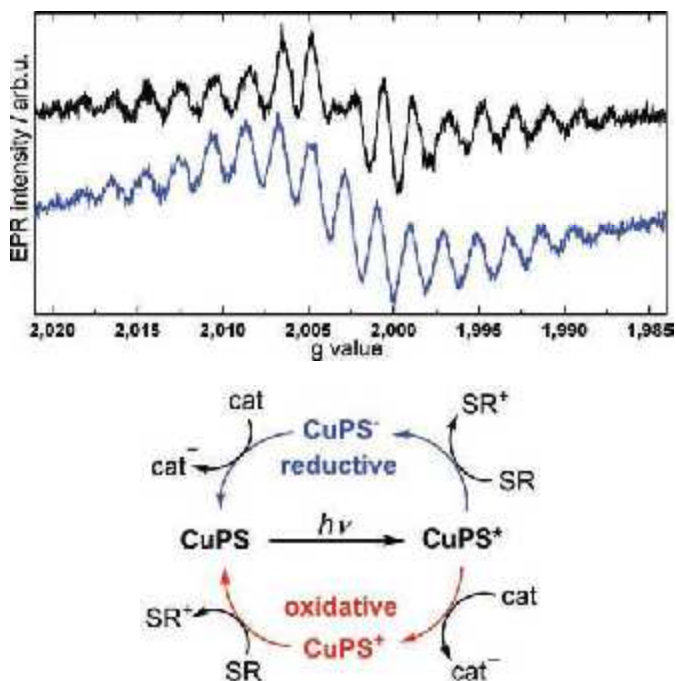

Fig. 6: Top: EPR spectrum of the singly reduced HET-1 obtained electrochemically at ~1.5 V vs. Ag/Ag⁺ (black) and photochemically under UV/vis irradiation with **triethylamine as sacrificial donor (blue). The resulting intermediate s excess electron is most likely located at the N^N ligand.** Bottom: general scheme of electron transfer processes from the excited photosensitizer (CuPS) to the water reduction catalyst (cat) by a reductive (blue) and an oxidative (red) pathway (SR = sacrificial reagent). The cat and the SR are necessary to take an electron from the excited CuPS or to provide an electron of the excited CuPS, respectively. In a **last step the protons are reduced by the catalyst to produce hydrogen.**

One option to stabilize the CuPS is its immobilization onto TiO_2 (powder or layer), which can be considered as first step towards a photoelectrochemical cell. Moreover, encapsulation with a polymer layer was performed to stabilize the composite. As a result, the catalysis time was twice as long and the obtained turnover number was increased by a factor of two. However, the mechanism is not clarified in detail and no emission could be detected. This is most likely due to the fast electron injection from the populated triplet excited state into the conduction band of TiO_2.[32]

INTERMOLECULAR PROCESSES   THE CATALYTIC UNIT

According to the results of the copper photosensitizers, the attention shifted to the catalytic center as well. This is important because the overall system only works with photosensitizer and catalyst and catalytic performance can be also improved at the part of the catalytic center. In the previous section $[Fe_3(CO)_{12}]$ attracted most attention due to its performance and abundance. In order to monitor changes during the catalysis in operation, *operando* IR spectroscopy was performed. Analysis of

the IR bands revealed that the starting material $[Fe_3(CO)_{12}]$ is directly converted to the hydride species $[HFe_3(CO)_{11}]^-$ (Fig. 7a), followed by the formation of a new species (Fig. 7b).[29] The formation of this bridged dinuclear iron complex is accompanied by an increased rate of hydrogen evolution, which implies that this process is coupled with the rate-limiting step.

The formed diiron species (Fig. 7b) strongly resembles the active site of [FeFe] hydrogenase enzymes,[33] which inspired a large community to mimic the catalytic center in structure and function.[11, 12] In nature, these enzymes reversibly catalyze hydrogen oxidation as well as proton reduction (Fig. 7c), and therefore, their mimics are widely used in photo- and electrocatalysis. A related diiron model complex was proven to successfully undergo proton reduction in the presence of a ruthenium photosensitizer and ascorbic acid as sacrificial electron donor.[34]

In the [FeFe] hydrogenase enzymes the reversible proton reduction and hydrogen oxidation reaction take place at the so-called distal iron (Fe_d), which possesses a free coordination sphere for substrate binding (Fig. 7c). Therefore, the synthesis of mononuclear [Fe] compounds that exclusively mimic this Fe_d (general structure Fig. 8, top) is a suitable method to investigate the underlying catalytic processes. Advantageously, these mononuclear iron model complexes offer multiple possibilities to fine-tune their electronic properties, and therefore, allow the investigation and understanding of structure-property-relationships. Thereby, information about the distal iron of [FeFe] hydrogenase active sites mimics are accessible. Specific variations can be made (cf. Fig. 8, top) at (i) the benzenedithiolate (bdt) bridge, (ii) the phosphine ligand(s) and (iii) the substituents at the amine function.[35]

The latter predominantly changes the basicity of the amine site, which serves as a potential proton shuttle from the nitrogen to the iron, while alterations of (ii) influence the structure of the complexes and changes of (i) and (ii) affect the metal s reduction potential. For instance, the nature of the phosphine ligand determines, whether hexa- or pentacoordinated mono iron complexes are obtained. For instance, monodentate lig-
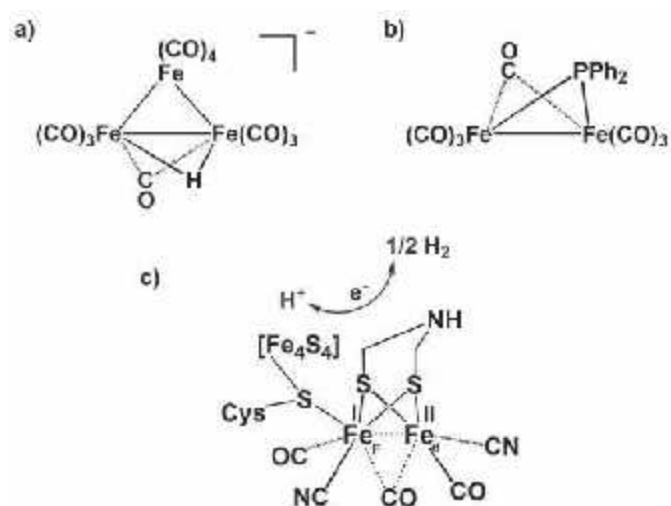

Fig. 7: a) Active species of the catalytic center generated from the starting material $[Fe_3(CO)_{12}]$ a short time after the start of the photocatalysis. b) During the reduction reaction this species is changed to a bridged Fe-Fe compound. c) General structure of a [FeFe] hydrogenase active site (p   proximal; d   distal).

ands like PMe_3 and PPh_3 result in hexacoordinated complexes. Instead, with bidentate ligands like 1,5-diaza-3,7-diphosphaoctane ($P^R_2N^{Ph}_2$) penta-coordinated [Fe] structures with a free coordination site are accessible (Fig. 8, top).[35]

In order to elucidate the mechanism the observation of catalytic intermediates of [Fe] during reduction and protonation events is desirable. For this reason, IR spectro-electrochemistry was applied and firstly showed the reversibility of reduction and re-oxidation in **Fe1** (Fig. 8, structure top right and spectrum bottom). Coupling of IR spectroscopy with electrochemistry is very supportive due to the indicative function of the carbonyl band, which provides information about the electron density at the iron center caused by π-π* backbonding. Upon several reduction and re-oxidation cycles depletion of the IR band at 1940 cm^{-1} occurs accompanied by the rise of a new band at 1850 cm^{-1}, which clearly evidences the reduction of the iron center of **Fe1**. Reduction increases the electron density at the iron, and thus, the backbonding leads to a stronger Fe-C bond. Accordingly, the C-O bond is weakened and the respective IR band shifts to lower wavenumbers. Moreover, the **Fe1** complex is stable over several reduction/re-oxidation cycles because no further changes in the corresponding IR spectra could be detected (Fig. 8, bottom), which is a very important prerequisite for electrochemical or photochemical hydrogen production. Moreover, the possibility

of hydrogen generation even in the presence of weak acids like acetic acid was confirmed by bulk electrolysis.[35]

Based on these results and in combination with the need for photoelectrolysis, attention was paid on the development of a photoelectrochemical cell. For this purpose, a [Fe] complex and a coumarin 343 dye were immobilized onto NiO. In the absence of any catalyst the coumarin 343 dye is reduced within femtoseconds by visible light and holes are generated at the NiO layer. Afterwards, the recombination of the separated charges between dye and p-type layer occurs within picoseconds.[36] Contrary, the immobilization of a [Fe] complex onto the dye-NiO surface results in a light-driven electron transfer from the primarily reduced coumarin 343 dye to the neighboring [Fe] within 50 ns, which is revealed by nanosecond transient absorption spectroscopy. Then, the recombination of the separated charges takes place within about 100 µs. With this experiment the electron hopping between different molecules on a NiO surface with the evidence of a reduced hydrogen evolving catalyst on NiO could be realized for the first time. The knowledge about such electron transfer processes is important for future design principles and operation requirements on the route to working photoelectrochemical cells.[37]

While iron systems already demonstrated to be very active reduction catalysts, systems based on copper also gained attention more recently. In combination with an iridium photosensitizer copper iodide showed a convincing long-term hydrogen evolution activity for more than 48 days. The nature of the real catalyst was examined using high angle annular dark field scanning transmission electron microscopy (HAADF-STEM) coupled with energy dispersive X-ray spectroscopy (EDX) and X-Ray absorption spectroscopy (XAS). The former revealed the formation of nanoparticles with sizes of 5-10 nm. EDX proved them to contain iridium and copper, however, the oxidation state could not entirely be determined with EDX. Therefore, XAS measurements were performed before and after catalysis, which confirmed the formation of Cu-Cu bonds, i.e. copper(0), during the catalysis.[38]

Thus, it becomes obvious that it is important to investigate the mechanism for every intermolecular system separately, because there is no unique mechanism and also homo- as well as heterogeneous pathways are possible.

CONCLUSION

In summary, light-driven proton reduction is achieved with several molecular systems. More importantly, a couple of methods have been adopted to investigate the underlying mechanisms, which is of particular significance for understanding and development of improved materials. Investigations focus either on the characterization of materials or the electron transfer processes. The electron transfer processes are resolved using transient absorption spectroscopy (femtosecond range) and resonance Raman spectroscopy (location of first excited state). Confirmation of singly reduced or oxidized states could be obtained by EPR spectroscopy and cyclovoltammetry (CV) as well as their combination. IR spectroscopy is a useful tool to study changes in molecular catalysts such as hydrogenase active
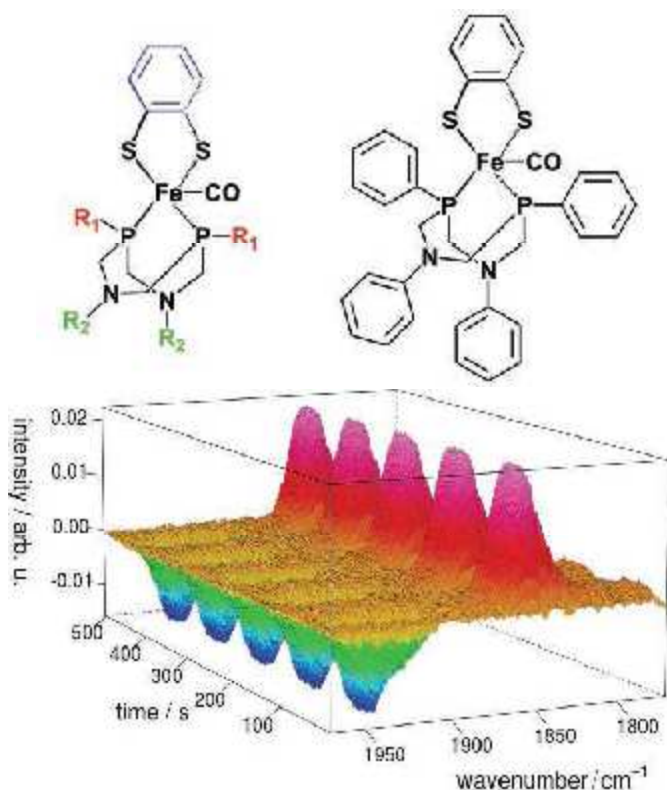

Fig. 8: Top left: General structure of model complexes of the distal Fe$_d$ of [FeFe] hydrogenases. The colors indicate various tuning possibilities to alter the geometric structure (blue and red), electronic properties (blue and red) and basicity (green) of these complexes. Top right: The complex Fe1 bearing phenyl groups at P (R$_1$) and N (R$_2$). Bottom: Fully reversible reduction (-1.8 V) and re-oxidation (-1.5 V vs. Ag/Ag$^+$) of Fe1 monitored by FTIR spectro-electrochemistry measured against the unreduced compound Fe1. As result, the original CO band of Fe1 at 1938 cm^{-1} depletes and a new band rises at 1850 cm^{-1} during the reduction. The re-oxidation processes lead to the unreduced Fe1 whereby no bands are detectable due to Fe1 is used as background. No loss or decomposition of the compound is detected during various cycles.

site mimics. In addition, coupling with CV yields information about stability of reduced and oxidized catalytic intermediates. In the case of conversion to heterogeneous materials, transmission electron microscopy (TEM) coupled with EDX provides insights into the size and elemental composition of the materials, while information about the oxidation state and environment are obtained with X-ray absorption near edge structure (XANES) and extended X-ray absorption fine structure (EXAFS). All these methods helped to deepen the understanding about electron transfer processes and materials properties, which will be also the prerequisite for the future development of advanced materials for water splitting.

ACKNOWLEDGEMENT

REFERENCES

[1]   N. S. Lewis, D. G. Nocera, *Proc. Natl. Acad. Sci. U. S. A.* 2006, **103**, 15729-15735.

[2]   M. A. Pellow, C. J. M. Emmott, C. J. Barnhart, S. M. Benson, *Energy Environ. Sci.* 2015, **8**, 1938-1952.

[3]   J. Barber, P. D. Tran, *J. R. Soc. Interface* 2013, **10**, 20120984.

[4]   C. Merschjann, S. Tschierlei, T. Tyborski, K. Kailasam, S. Orthmann, D. Hollmann, T. Schedel-Niedrig, A. Thomas, S. Lochbrunner, *Adv. Mater.* 2015, accepted, doi: 10.1002/adma.201503448

[5]   R. Marschall, *Top. Curr. Chem.* 2016, **371**, 143-172.

[6]   S. Campagna, F. Puntoriero, F. Nastasi, G. Bergamini, V. Balzani, *Top. Curr. Chem.* 2007, **280**, 117-214.

[7]   L. Flamigni, A. Barbieri, C. Sabatini, B. Ventura, F. Barigelletti, *Top. Curr. Chem.* 2007, **281**, 143-204.

[8]   M. Schulz, M. Karnahl, M. Schwalbe, J. G. Vos, *Coord. Chem. Rev.* 2012, **256**, 1682-1705.

[9]   M. S. Lazorski, F. N. Castellano, *Polyhedron* 2014, **82**, 57-70.

[10] V. Artero, M. Chavarot-Kerlidou, M. Fontecave, *Angew. Chem.* 2011, **123**, 7376-7405; *Angew. Chem. Int. Ed.* 2011, **50**, 7238-7266.

[11] C. Tard, C.J. Pickett, *Chem. Rev.* 2009, **109**, 2245-2274.

[12] S. Tschierlei, S. Ott, R. Lomoth, *Energy Environ. Sci.* 2011, **4**, 2340-2352.

[13] S. Rau, B. Schäfer, D. Gleich, E. Anders, M. Rudolph, M. Friedrich, H. Görls, W. Henry, J. G. Vos, *Angew. Chem.* 2006, **118**, 6361-6364.

[14] S. Tschierlei, M. Karnahl, M. Presselt, B. Dietzek, J. Guthmuller, L. González, M. Schmitt, S. Rau, J. Popp, *Angew. Chem.* 2010, **122**, 4073-4076.

[15] M. Wächtler, J. Guthmuller, L. González, B. Dietzek, *Coord. Chem. Rev.* 2012, **256**, 1479-1508.

[16] S. Tschierlei, M. Presselt, C. Kuhnt, A. Yartsev, T. Pascher, V. Sundström, M. Karnahl, M. Schwalbe, B. Schäfer, S. Rau, M. Schmitt, B. Dietzek, J. Popp, *Chem. Eur. J.* 2009, **15**, 7678-7688.

[17] M. G. Pfeffer, B. Schäfer, G. Smolentsev, J. Uhlig, E. Nazarenko, J. Guthmuller, C. Kuhnt, M. Wächtler, B. Dietzek, V. Sundström, S. Rau, *Angew. Chem. Int. Ed.* 2015, **54**, 5044-5048.

[18] M. G. Pfeffer, T. Kowacs, M. Wächtler, J. Guthmuller, B. Dietzek, J. G. Vos, S. Rau, *Angew. Chem. Int. Ed.* 2015, **54**, 6627-6631.

[19] L. Zedler, J. Guthmuller, I. Rabelo de Moraes, S. Kupfer, S. Krieck, M. Schmitt, J. Popp, S. Rau, B. Dietzek, *Chem. Commun.* 2014, **50**, 5227-5229.

[20] T. D. Pilz, N. Rockstroh, S. Rau, *J. Coord. Chem.* 2010, **63**, 2727-2742.

[21] K. Heussner, K. Peuntinger, N. Rockstroh, L. C. Nye, I. Ivanovic-Burmazovic, S. Rau, C. Streb, *Chem. Commun.* 2011, **47**, 6852-6854.

[22] K. Heussner, K. Peuntinger, N. Rockstroh, S. Rau, C. Streb, *Dalton Trans.* 2015, **44**, 330-337.

[23] N. Armaroli, *Chem. Soc. Rev.* 2001, **30**, 113-124.

[24] M. W. Mara, K. A. Fransted, L. X. Chen, *Coord. Chem. Rev.* 2015, **282-283**, 2-18.

[24] S.-P. Luo, E. Mejía, A. Friedrich, A. Pazidis, H. Junge, A.-E. Surkus, R. Jackstell, S. Denurra, S. Gladiali, S. Lochbrunner, M. Beller, *Angew. Chem.* 2013, **125**, 437-441.

[25] R. S. Khnayzer, C. E. McCusker, B. S. Olaiya, F. N. Castellano, *J. Am. Chem. Soc.* 2013, **135**, 14068-14070.

[26] S. Tschierlei, M. Karnahl, N. Rockstroh, H. Junge, M. Beller, S. Lochbrunner, *ChemPhysChem* 2014, **15**, 3709-3713.

[27] E. Mejía, S.-P. Luo, M. Karnahl, A. Friedrich, S. Tschierlei, A.-E. Surkus, H. Junge, S. Gladiali, S. Lochbrunner, M. Beller, *Chem. Eur. J.* 2013, **19**, 15972-15978.

[28] M. Iwamura, S. Takeuchi, T. Tahara, *Acc. Chem. Res.* 2015, **48**, 782-791.

[29] S. Fischer, D. Hollmann, S. Tschierlei, M. Karnahl, N. Rockstroh, E. Barsch, P. Schwarzbach, S.-P. Luo, H. Junge, M. Beller, S. Lochbrunner, R. Ludwig, A. Brückner, *ACS Catal.* 2014, **4**, 1845-1849.

[30] S. I. Bokarev, D. Hollmann, A. Pazidis, A. Neubauer, J. Radnik, O. Kühn, S. Lochbrunner, H. Junge, M. Beller, A. Brückner, *Phys. Chem. Chem. Phys.* 2014, **16**, 4789-4796.

[31] A. Kaeser, M. Mohankumar, J. Mohanraj, F. Monti, M. Holler, J.-J. Cid, O. Moudam, I. Nierengarten, L. Karmazin-Brelot, C. Duhayon, B. Delavaux-Nicot, N. Armaroli, J.-F. Nierengarten, *Inorg. Chem.* 2013, **52**, 12140-12151.

[32] M. Karnahl, E. Mejía, N. Rockstroh, S. Tschierlei, S.-P. Luo, K. Grabow, A. Kruth, V. Brüser, H. Junge, S. Lochbrunner, M. Beller, *ChemCatChem* 2014, **6**, 82-86.

[33] W. Lubitz, H. Ogata, O Rüdiger, E. Reijerse, *Chem. Rev.* 2014, **114(8)**, 4081-4148.

[34] D. Streich, Y. Astuti, M. Orlandi, L. Schwartz, R. Lomoth, S. Ott, L. Hammarström, *Chem. Eur. J.* 2010, **16**, 60-63.

[35] A. Orthaber, M. Karnahl, S. Tschierlei, D. Streich, M. Stein, S. Ott, *Dalton Trans.* 2014, **43**, 4537-4549.

[36] A. Morandeira, G. Boschloo, A. Hagfeldt, L. Hammarström, *J. Phys. Chem. C* 2008, **112**, 9530-9537.

[37] J. M. Gardner, M. Beyler, M. Karnahl, S. Tschierlei, S. Ott, L. Hammarström, *J. Am. Chem. Soc.* 2012, **134**, 19322-19325.

[38] H. Junge, Z. Codolà, A. Kammer, N. Rockstroh, M. Karnahl, S.-P. Luo, M.-M. Pohl, J. Radnik, S. Gatla, S. Wohlrab, J. Lloret, M. Costas, M. Beller, *J. Mol. Catal. A Chem.* 2014, **395**, 449-456.

Tobias Weller, Pascal Voepel, Roland Marschall*

CHARGE CARRIER TRANSFER IN HETEROGENEOUS PHOTOCATALYSIS

Ternary and quaternary oxide semiconductors with tunnel- or layer-type crystal structure, e.g. defect-pyrochlores or layered perovskites, offer unique properties for band gap engineering while being stable under light irradiation. Besides band gap reduction, minimizing charge carrier recombination in such materials is very important to improve the overall photocatalytic performance. Different strategies to optimize charge carrier transfer are presented and discussed, using complex mixed oxides and novel composites as model systems.

INTRODUCTION

Heterogeneous photocatalysis utilizes irradiated photons to excite charge carriers in semiconductor materials, which can perform electrochemical oxidation and reduction reactions on the surface of the semiconductor. The type of reaction possible depends on the electrochemical redox potential of each reaction with respect to the position of valence band (VB) and conduction band (CB) of the semiconductor.[1] For example, to split water photocatalytically into Hydrogen (H_2) and Oxygen (O_2), the CB minimum of the semiconductor has to be more negative than 0 V (H^+/H_2, pH=0), and the VB maximum has to be more positive than 1.23 V (H_2O/O_2, pH=0). A minimum band gap of 1.23 eV is the result, however due to overpotentials necessary and ohmic losses, optimum band gaps for single absorber materials in photoelectrochemical water splitting are discussed in the range of 1.8 to 2.2 eV.[2,3]

Charge carriers, namely electrons and holes, excited in a semiconductor have to reach the surface first in order to perform the surface reduction or oxidation, respectively.[4] During that migration, they most probably recombine if their diffusion length L_d is shorter than the light penetration and depletion layer width combined,[5] and/or e.g. at crystal defects or grain boundaries.[3] Recombination reduces the photocatalytic or photoelectrochemical performance, thus different strategies are investigated to improve charge carrier separation, lifetime, and migration, while reducing recombination.

A very prominent example is the decoration of semiconductors with noble metals, acting as co-catalysts and active sites.[6] They promote charge separation via transfer across the formed

junction between metal and semiconductor, e.g. via Schottky contact, and can also act as electron reservoir for the reduction reaction. By that, the lifetime of the charge carriers is strongly enhanced, meaning that less recombination takes place and more charge carriers are longer available for reaction. Typical noble metals used as co-catalyst are Platinum (Pt), Gold (Au) and Rhodium (Rh). Several research groups investigate the substitution of such noble metals with more abundant catalysts for either H_2 or O_2 evolution.[7,8]

STRUCTURING THE SEMICONDUCTOR

Despite modifying the surface of the light-absorbing semiconductor, shortened diffusion pathways, improved charge carrier lifetimes, or better charge carrier separation can be achieved also by mesostructuring. One strategy is the synthesis and in-situ formation of semiconductor multiphase or multicomponent heterojunctions, to reduce charge carrier recombination due to vectorial charge transfer in photocatalytic materials or photoelectrochemical devices.
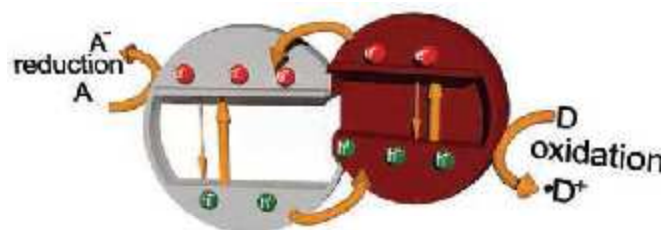

Fig. 1: Schematic charge carrier excitation, recombination, and transfer in a two-component semiconductor heterojunction.

Figure 1 shows the principle, depicting two n-type semiconductors with different band gaps, which are however both excited by irradiated light (not shown). In both semiconductors, electron-hole pairs are generated by excitation of electrons from the VB to the CB, shown by the thick vertical arrows. The thin arrows indicate the possibility of charge carrier recombination. When both semiconductors are in good contact, electrons can be transferred to the semiconductor with the lower lying CB while holes can move upwards from the lower lying VB to the other. Thus, the photoexcited charges are separated, and the recombination of electrons and holes across the two materials is less probable. Figure 1 also shows the possible following surface reactions, the oxidation occurring at the semiconductor with the higher VB, and the reduction at the semiconductor with the lower CB.

* Dr. Roland Marschall
Institute of Physical Chemistry, Justus-Liebig-University Giessen
Heinrich-Buff-Ring 17, 35392 Giessen, Germany
phone: +49-641-9934592, fax: +49-641-9934599
E-Mail: roland.marschall@phys.Chemie.uni-giessen.de

This type of band position alignment is called a type II hetero-junction. For comparison, in type I heterojunctions the VB and CB edges of one semiconductor are enclosed by the VB and CB edges of the second semiconductor. Type III heterojunctions have comparable band alignment to Figure 1, however the higher lying VB edge is even more cathodic than the CB minimum of the other semiconductor.[9]

It is also noteworthy that by semiconductor heterojunctions the absorption of the photocatalyst system can be increased. In Figure 1, the red sphere depicts a semiconductor with a smaller band gap than the grey sphere. The color indicates that only the red semiconductor can absorb visible light, while the grey one can absorb only UV light due to its larger band gap. When the heterojunction is irradiated with sunlight, which contains ≈5% UV light, charge carriers are generated in both components. Without the red semiconductor, the left particle would only be able to utilize those ≈5% for photocatalysis, but with the red semiconductor more photons from sunlight in the visible light range can be absorbed by the material system, leading to more generated charge carriers for photocatalysis. In addition, those charge carriers are also separated, as described before.

To enable efficient interfacial contact in semiconductor composites, several strategies can be followed to achieve intimate interfacial contact between the different components on the nanoscale.

While physical mixtures of preformed components have often been shown to exhibit insufficient interfacial contact,[10] methods like high-energy ball milling or ultrasonication can be used to improve it. However, the most efficient strategies to prepare multiphase or multicomponent heterojunctions usually include the in-situ formation of one component in the presence of a second, or the synthesis of both components simultaneously. For example, TiO_2-polyheptazine heterojunctions are prepared via formation of polyheptazine in the presence of preformed TiO_2 particles.[11] In contrast, brookite-anatase TiO_2 multiphase heterojunctions are prepared by controlling the urea concentration for thermal hydrolysis of titanium bis(ammonium lactate) dihydroxide (TALH) under hydrothermal conditions.[12]

By adjusting the precursor concentration and ratio during wet chemical synthesis, it is possible to control the formation and component composition of the semiconductor heterojunction. For instance, by setting the ratio of Barium (Ba) and Tantalum (Ta) precursors to desired amounts, two- and three-component heterojunctions of $Ba_5Ta_4O_{15}$, $Ba_3Ta_5O_{15}$ and $BaTa_2O_6$ can be prepared in-situ.[13] $Ba_5Ta_4O_{15}$ has a layered perovskite structure that is beneficial for nitrogen doping via ammonolysis to reduce its band gap into the visible light range.[14] Already an optimum two-component heterojunction of $Ba_5Ta_4O_{15}$ and $Ba_3Ta_5O_{15}$ shows improved activity towards H_2 generation from water/methanol mixtures. Interestingly, this two-component heterojunction already shows comparable H_2 evolution activity without any co-catalyst to phase-pure $Ba_5Ta_4O_{15}$ with photodeposited Rh co-catalyst (Figure 2).

Moreover, the difference in H_2 evolution rates before (■) and after (●) Rh photodeposition is much larger for phase pure $Ba_5Ta_4O_{15}$ than with $Ba_5Ta_4O_{15}$-$Ba_3Ta_5O_{15}$. For the phase pure
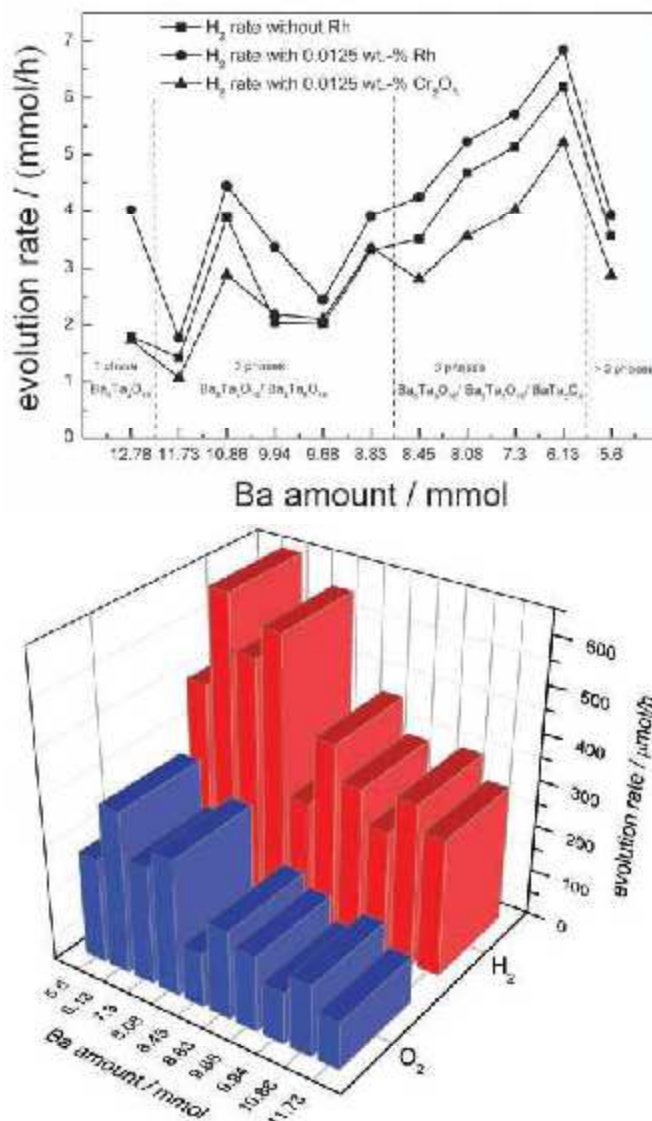

Fig. 2: Top: H_2 evolution experiments with different Barium tantalate heterojunctions in H_2O/MeOH before and after deposition of Rh co-catalyst as well as photodeposition of Cr_2O_3; Bottom: Overall water splitting with Rh/Cr_2O_3-decorated Barium tantalate heterojunctions; Reproduced with permission[13], © 2014, Published by The Royal Society of Chemistry.

material, the co-catalyst is the only possibility to separate photoexcited charges, transferring electrons to the noble metal active site to reduce recombination. In the heterojunction, the composite itself separates the charges already reducing the recombination, thus additional co-catalyst deposition has a minor effect on charge separation and activity.

When the optimum three-component heterojunction is prepared with a Ba/Ta ratio of 0.6 (denoted Ba amount 6.13 mmol), an even more astonishing fact can be observed. The heterojunction made of $Ba_5Ta_4O_{15}$-$Ba_3Ta_5O_{15}$-$BaTa_2O_6$ without Rh shows 50 % higher activity for H_2 evolution than the phase pure $Ba_5Ta_4O_{15}$ with Rh on the surface. The trend of improved photocatalytic activity can also be transferred to overall water splitting after covering Rh with Cr_2O_3 (Figure 2 bottom). However, the values for H_2 are lower in that case since now water has to be oxidized instead of methanol, being the rate determining step due to the overpotential of O_2 at the oxide surface. This

could be further optimized with an additional co-catalyst. Cr_2O_3 is used to cover Rh to inhibit the back reaction of O_2 and H_2 to water, since O_2 cannot diffuse through Cr_2O_3 for back reaction at the Rh surface.[15]

The results indicate that composite design can be more efficient for charge carrier separation than the use of noble metal co-catalysts. However, it also shows that phase purity should be of utmost concern for material scientists in the field of semiconductor photocatalysis, because impurities can boost photocatalytic activity due to charge carrier separation and transfer to a level phase pure materials would not achieve. Figure 3 shows the possible charge carrier transfer *via* the three-component composite. This transfer is only that efficient since the three components have very intimate interfacial contact due to the *in-situ* formation during synthesis.
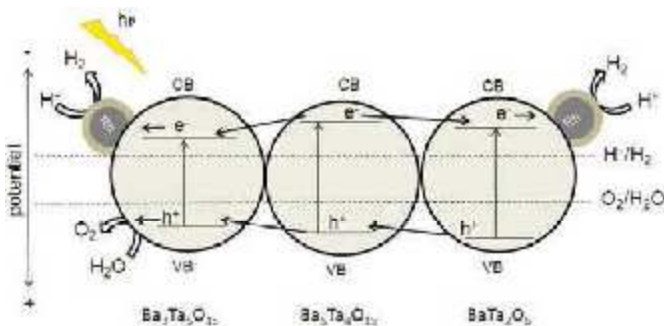

Fig. 3: Possible charge transfer across the three-component heterojunction in overall water splitting; Reproduced with permission[13], © 2014, Published by The Royal Society of Chemistry.

The examples shown are heterojunctions between two or more n-type semiconductors. However, the situation is different when the heterojunction is made of a p-type and an n-type semiconductor. Semiconductor physics dictates that between two semiconductors in contact Fermi level equilibration occurs. In case of p-n junctions, the effect of Fermi level equilibration results in strong band bending in the space charge layer between both semiconductors. Under irradiation, photoexcited electrons would always transfer from the p-type to the n-type semiconductor, while the holes transfer to the p-type semiconductor, independent on the band positions before the formation of the heterojunction.

A classic example is the combination of Cu_2O, a p-type semiconductor, and TiO_2, an n-type semiconductor.[16] More recent examples of p-n-heterojunction photoelectrodes utilize two visible-light absorbing semiconductors, for example, p-$CaFe_2O_4$/ TaON or p-$CaFe_2O_4$/α-Fe_2O_3.[17,18] The examples of p-n oxide heterojunctions are still quite rare, compared to the number of n-n heterojunctions known, since not many p-type oxide semiconductor have yet been considered.[9] However, p-n heterojunctions are very efficient for charge separation, and can open up new ways of vectorial charge transfer in future composites.

REDUCING THE DIFFUSION LENGTH

Fibrous semiconductors can be advantageous compared to particle systems in semiconductor photocatalysis, if having a

high aspect ratio and surface area for good photocatalytic activity, but remaining thick enough avoiding band gap increase due to quantum confinement.[19] Thus, the diffusion length for charge carriers is decreased, which should reduce the recombination probability.

A prominent technique to prepare semiconductor nanofibers from solutions is electrospinning. Molecular metal precursors are dissolved in appropriate solvents containing a polymer to increase the viscosity and prevent Rayleigh instability. This spinning solution is pumped through a cannula, which also acts as electrode. Between the cannula and a collector, a high voltage is applied.[20] Fibers are collected containing usually around 70% polymer, resulting in oxide nanofibers after calcination.

Even the complex semiconductor materials $Ba_5Ta_{4-x}Nb_xO_{15}$ (x=0, 2, 4) can be prepared *via* electrospinning as nanofibers with several micrometers in length. Although these (111)-layered perovskite fibers need calcination temperatures of 800 - 900 °C, the fibrous morphology can still be achieved with a highly crystalline material (Figure 4) consisting of small single crystals. The reason is the formation mechanism *via* intermediately formed carbonates strengthening the fiber morphology.[21] The different materials exhibit similar surface areas of 5 $m^2 g^{-1}$.

All the fibers are active in overall water splitting. However, H_2 and O_2 evolution is not stoichiometric for $Ba_5Ta_4O_{15}$ and $Ba_5Ta_2Nb_2O_{15}$, which might be due to not fully covered Rh by Cr_2O_3. However, the nanofibers do not show superior photocatalytic activity in water splitting compared to powders prepared *via* sol-gel syntheses. This fact has to be investigated further by optimizing the fiber diameter and surface area.

Is there an optimum morphology for photocatalysis? The nanofiber example shows that sometimes one cannot foresee the influence of morphology on photocatalytic properties, especially not for such complex materials. However, what is the optimum morphology for a high surface area photocatalyst?

To achieve high surface area oxide materials, templating strategies are known for decades utilizing surfactants, block-copolymers or hard templates to prepare highly mesoporous (pores between 2 - 50 nm) materials. In many cases, even ordered mesoporosity is achieved, due to self assembly, liquid-crystal templating, or nanocasting.[22,23] Besides porosity, the preparation of nanoparticles is another possibility to increase the surface area of an oxide semiconductor.

It is very important to know and understand the optimum morphology of high surface area semiconductors for photocatalysis, whether it should be non-ordered but porous, highly ordered and porous, or as nanoparticles. Figure 5 shows three possible schematic morphologies plus some examples. All three morphologies should exhibit high surface area and short diffusion lengths for photoexcited charge carriers, the latter due to small particle size or thin pore walls, usually in the range of several nanometers.

It is already known from other applications where transport phenomena have to be considered (e.g. in catalysis) that
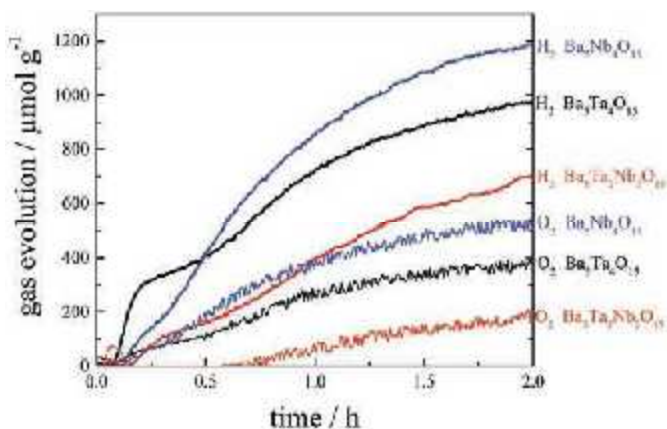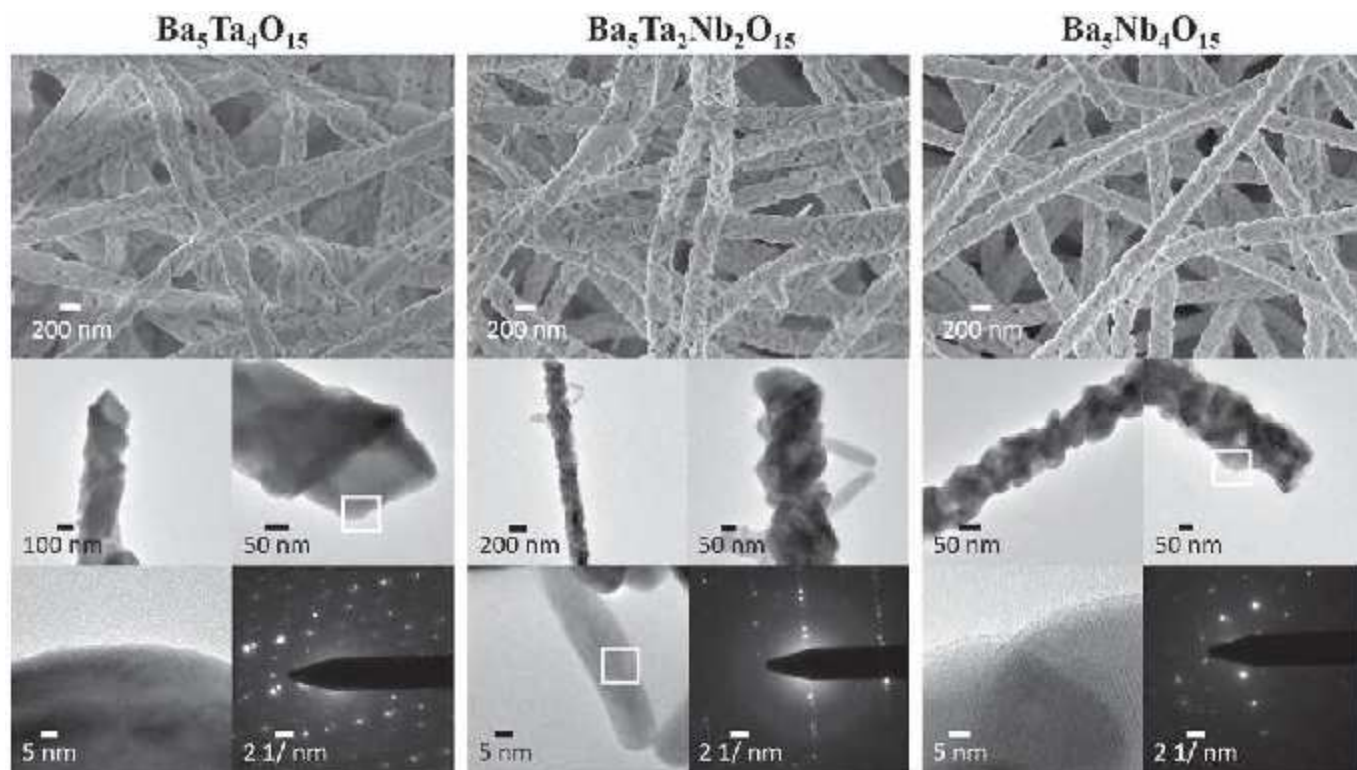
Fig. 4: Top: SEM (top row) and TEM (middle row) images of layered perovskite nanofibers after calcination at 900 °C, plus SAED (lower row) of the marked areas. Bottom: Overall water splitting gas evolution traces of (111)-layered nanofibers with Rh/Cr₂O₃ (0.0125 wt.-% each) decoration. Reproduced with permission [19], © 2015 Wiley-VCH.

pore disorder can be crucial to reduce pore blocking effects and transport constraints.[25] Highly ordered narrow pores, like in hexagonal ordered mesopores (Figure 5 middle column), can be easily blocked, while a non-ordered porosity exhibits many different types of pore channels. Thus, it is questionable whether an ordered porous material would be beneficial for photocatalysis, but still be worthwhile as a model system.

Comparing mesoporous semiconductors with nanoparticles for H_2 evolution, different studies have been performed on Pt-decorated TiO_2.[26] Mesoporous TiO_2 with ordered mesopores of 7.2 nm prepared at 350 °C showed the highest surface area (267 m² g⁻¹), but hardly any crystallinity and very low activity. With increasing crystallinity *via* calcination at higher temperatures (400 or 450 °C), the mesopore structural ordering and

the surface area decreased (209 and 175 m² g⁻¹), the pore diameter decreased slightly, but the activity increased, respectively. Commercial TiO_2 nanoparticles (Evonik-Degussa Aeroxide TiO_2 P25) however exhibited only 50 m² g⁻¹ of specific surface area, are highly crystalline, but show lower activity than mesoporous TiO_2 prepared at 400 °C.

This study revealed that high crystallinity is more important for photocatalytic hydrogen generation than surface area. However, what if the crystallinity would be comparably high, but the pore morphology is varied? Highly ordered mesoporous SiO_2 or TiO_2 materials are usually amorphous materials. However, a photocatalyst should exhibit high crystallinity with low defect concentration to minimize recombination. The latter seems really necessary even if the diffusion path for the charge carriers is only 5-10 nm. But is high surface area or high pore ordering or the pore diameter the most important parameter for high photocatalytic activity?

We use the complex semiconductor $CsTaWO_6$ as model system to investigate the optimum pore morphology for H_2 production. $CsTaWO_6$ has a defect-pyrochlore structure that is, like the layered structures of $Ba_5Ta_{4-x}Nb_xO_{15}$, beneficial for nitrogen doping *via* ammonolysis to reduce the band gap into the visible light range.[27] The two d⁰ elements also enable band gap engineering *via* lattice variations,[28] and we have developed a citrate-based aqueous synthesis route for this material,[29] which now enables us to investigate mesostructuring of this compound. We have succeeded to prepare highly porous, highly crystalline $CsTaWO_6$ with different pore sizes and morphology, however not with highly ordered mesopores yet.[30] We found first indications for a dependence of photocatalytic H_2 generation on pore morphology, but more studies have to be performed to confirm these findings. We will also compare our mesoporous $CsTaWO_6$ ma-

terials with highly crystalline, phase-pure nano-
particles (compare Figure 5) in the future.

CONCLUSIONS

Different strategies have been presented to im-
proved charge carrier transfer in photocatalysis,
in order to reduce recombination and increase
photocatalytic activity. Semiconductor hetero-
junctions improve charge carrier separation that
reduces recombination probability. Mesostruc-
tured semiconductors like high surface area
mesoporous or nanoparticulate materials can be
achieved in order to reduce charge carrier diffu-
sion pathways. It is not clear yet which strategy is
the most efficient. However, there are also hard-
ly any examples combining different strategies,
e.g. composite nanofibers/nanoparticles, which
might lead to further improved performance in photocatalysis
and photoelectrochemistry. Nevertheless, combining materials
research with physicochemical characterization methods will re-
veal the optimum combination of morphology and mesostructure
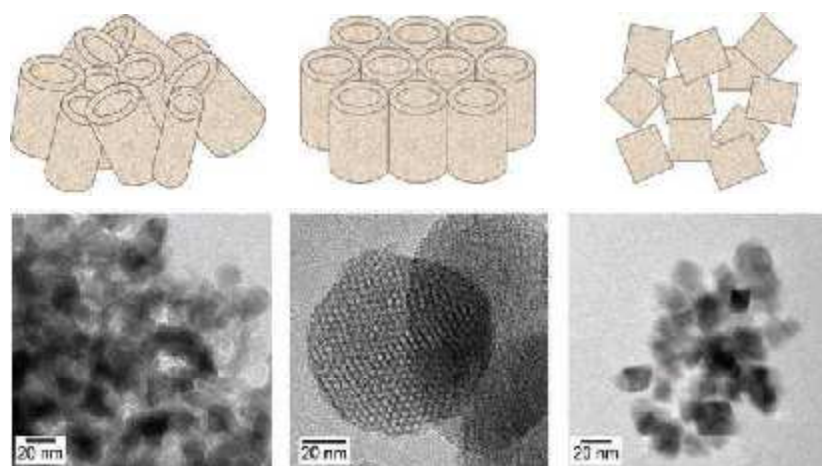for increased charge carrier lifetimes and improved performance.

Fig. 5: Upper row schematics: Non-ordered porosity vs. ordered porosity vs. nanoparticles; Below: Non-ordered mesoporous $CsTaWO_6$ prepared by the authors, highly ordered mesoporous SiO_2 prepared by [24], and $CsTaWO_6$ nanoparticles also prepared by the authors. TEM of SiO_2 reproduced with permission[24], © 2009 Wiley-VCH.

ACKNOWLEDGEMENT

REFERENCES

1   Hoffmann, M. R.; Martin, S.T.; Choi, W.; Bahnemann, D. W.;
    Chem. Rev. 1995, **95** (1), 69-96.

2   Seitz, L. C.; Chen, Z.; Forman, A. J.; Pinaud, B. A.; Benck, J. D.;
    Jaramillo, T.F.; *Chem. Sus. Chem.* 2014, **7** (5), 1372-1385.

3   Pinaud, B. A.; Benck, J. D.; Seitz, L. C.; Forman, A. J.; Chen, Z.;
    Deutsch, T. G.; James, B. D.; Baum, K. N.; Baum, G. N.; Ardo, S.;
    Wang, H.; Miller, E.; Jaramillo, T. F.; *Energy Environ. Sci.* 2013, **6**
    (7), 1983-2002.

4   Kudo, A.; Miseki, Y.; *Chem. Soc. Rev.* 2009, **38** (1), 253-278.

5   Van de Krol, R.; Grätzel, M.; in *Photoelectrochemical Hydrogen
    Production*, Springer, 2012.

6   Yang, J.; Wang, D.; Han, H.; Li, C.; *Acc. Chem. Res.* 2013, **46** (8),
    1900-1909.

7   Kanan, M. W.; Nocera, D. G.; *Science* 2008, **321** (5892), 1072-
    1075.

8   Busser, G. W.; Mei, B.; Weide, P.; Vesborg, P. C. K.; Stühren-
    berg, K.; Bauer, M.; Huang, X.; Willinger, M.-G.; Chrokendorff, I.;
    Schlögl, R.; Muhler, M.; *ACS Catal.* 2015, **5** (9), 5530-5539.

9   Marschall, R.; *Adv. Funct. Mater.* 2014, **24** (17), 2421-2440.

10 Kho, Y.K.; Iwase, A.; Teoh, W.Y.; Mädler, L.; Kudo, A.; Amal, R.; *J.
    Phys. Chem. C* 2010, **114** (6), 2821-2829.

11 Bledowski, M.; Wang, L.;, Ramakrishnan, A.;, Khavryuchenko,
    O.V.; Khavryuchenko, V.D.; Ricci, P.C.; Strunk, J.; Cremer, T.;
    Kolbeck, C.; Beránek, R.; *Phys. Chem. Chem. Phys.* 2011, **13**
    (48), 21511-21519.

12 Kandiel, T.A.; Feldhoff, A.; Robben, L.; Dillert, R.; Bahnemann,
    D.W.; *Chem. Mater.* 2010, **22** (6), 2050-2060.

13 Soldat, J.; Marschall, R.; Wark, M.; *Chem. Sci.* 2014, **5** (10)
    3746-3752.

14 Mukherji, A.; Sun, C.; Smith, S. C.; Lu, G. Q.; Wang, L.; *J. Phys.
    Chem. C* 2011, **115** (31), 15674-15678.

15 Maeda, K.; Domen, K.; *J. Phys. Chem. Lett.* 2010, **1** (18), 2655-
    2661.

16 Zhang, J.; Zhu, H.; Zheng, S.; Pan, F.; Wang, T.; *ACS Appl. Mater.
    Interfaces* 2009, **1** (10), 2111-2114.

17 Kim, E. S.; Nishimura, N.; Magesh, G.; Kim, J. Y.; Jang, J.-W.; Jun,
    H.; Kubota, J.; Domen, K.; Lee, J. S.; *J. Am. Chem. Soc.* 2013,
    135 (14), 5375-5383.

18 Ahmed, M. G.; Kandiel, T. A.; Ahmed, A. Y.; Kretschmer, I.;
    Rashwan, F.; Bahnemann, D.; *J. Phys. Chem. C* 2015, **119** (11),
    5864-5871.

19 Bahnemann, D. W.; Kormann, C.; Hoffmann, M. R.; *J. Phys.
    Chem.* 1987, **91** (14), 3789-3798.

20 Greiner, A.; Wendorff, J. H.; *Angew. Chem. Int. Ed.* 2007, **46**
    (30), 5670-5703.

21 Hildebrandt, N. C.; Soldat, J.; Marschall, R.; *Small* 2015, **11**
    (17), 2051-2057.

22 Li, W.; Zhao, D.Y.; *Chem. Commun.* 2013, **49** (10), 943-946.

23 Gu, D.; Schüth, F.; *Chem. Soc. Rev.* 2014, **43** (1), 313-344.

24 Marschall, R.; Bannat, I.; Feldhoff, A.; Wang, L.; Lu, G. Q.; Wark,
    M.; *Small* 2009, **5** (7), 854-859.

25 Rolison, D. R.; *Science* 2003, **299** (5613), 1698-1701.

26 (a) Kandiel, T. A.; Ismail, A. A.; Bahnemann, D. W.; *Phys. Chem.
    Chem. Phys.* 2011, **13** (45), 20155-20161; (b) Kandiel, T. A.;
    Dillert, R.; Robben, L.; Bahnemann, D. W., *Catal. Today* 2011,
    161 (1), 196-201.

27 Mukherji, A.; Marschall, R.; Tanksale, A.; Sun, C.; Smith, S. C.;
    Lu, G. Q.; Wang, L.; *Adv. Funct. Mater.* 2011, **21** (1), 126-132.

28 Schwertmann, L.; Grünert, A.; Pougin, A.; Sun, C.; Wark, M.;
    Marschall, M.; *Adv. Funct. Mater.* 2015, **25** (6), 905-912.

29 Schwertmann, L.; Wark, M.; Marschall, R.; *RSC Adv.* 2013, **3**
    (41), 18908-18915.

30 Weller, T.; Sann, J.; Marschall, R.; unpublished results.